State-selected photodissociation dynamics: Complete characterization of the OH fragment ejected by the HONO $\tilde{A}$ state

R. Vasudev and R. N. Zare
Department of Chemistry, Stanford University, Stanford, California 94305

R. N. Dixon
School of Chemistry, University of Bristol, Bristol BS8 1TS, United Kingdom

(Received 3 October 1983; accepted 14 December 1983)

Trans-HONO is optically prepared in specific $-N=O$ stretching vibrational levels (2^n, $n = 1,2,3$) of the $\tilde{A}$ state at 369, 355, and 342 nm. The ejected OH fragment is completely characterized by Doppler and polarization laser excitation spectroscopy. In this manner the OH translational energy, angular distribution, rotational alignment, and internal state distribution (vibration, rotation, spin-orbit and Λ-doubling components) are probed through the OH A–X system. The OH fragment is found to be translationally hot (~ 0.5 eV) with a nearly $\sin^2\theta$ angular distribution about the electric vector of the photolysis laser. The corresponding line shapes are Doppler split. However, the line shapes and widths do not noticeably depend on either fragment rotation or parent vibration. The internal motion of the OH fragment is vibrationally and rotationally cold; the spin-orbit components and the Λ doublets are not in equilibrium. The OH fragment is aligned and its π lobe lies preferentially in the plane of rotation. With increasing rotational excitation, these effects become more pronounced. This information allows us to construct a detailed photodissociation mechanism. The fragmentation is prompt and the trajectories of the recoiling fragments lie close to the initial HONO plane. The impulse associated with the central O–N bond fission contributes predominantly to OH translation while the rotation appears to arise from the zero-point motion of the parent in-plane bending and torsional vibrations. The OH energy content is found to be quite insensitive to the parent ν_2 vibration, suggesting that the $\tilde{A}$ state surface is rather "flat" along the $-N=O$ stretch compared to the steep fragmentation coordinate.

I. INTRODUCTION

Molecular dissociation is a primary chemical event and has thus attracted considerable experimental[1,2] and theoretical[3–8] interest. Typical recent photodissociation experiments may be roughly classified into two types. The first of these seeks to elucidate the dissociation/predissociation mechanism through, e.g., measurements of spectral line broadening[9–12] or fluorescence lifetime[13] as a function of the excited state quantum numbers. The second of these seeks to probe the fate of the ejected nascent photofragments following the optical preparation of the parent excited state.[2] The overall details of the dynamics of a photodissociation process depend on the lifetime, geometry, and the force field of the parent molecule, the nature of the intramolecular interactions, and exit-channel interactions between the recoiling fragments. When the parent is photoselected by a polarized laser beam, the optical transition moment is preferentially aligned along the $\hat{\epsilon}$ vector of the exciting radiation. This spatial alignment results in anisotropic photofragment angular distributions. In addition, if the fragmentation is faster than molecular rotation, the parent alignment is almost completely transferred to that of the products.

In an ideal photodissociation experiment, one would like to measure, for a given fully defined ("$vJKM$") parent state, the product distribution as a function of all the internal quantum numbers (v,J,M,Ω, etc.), as well as the translational motion and its anisotropy. However, most of the past photodissociation experiments have involved the measurements of only one of either (a) fragment vectorial properties such as angular distributions through mass spectrometry and recoil velocities by time-of-flight mass analysis[1,14]; or (b) product overall scalar properties such as internal state distributions. The former technique, of course, is not very sensitive to the internal states. If a photofragment is electronically excited, the desired goal may be partly accomplished by dispersing its emission.[2] When the fragment is electronically unexcited, the internal state distribution can be determined through, e.g., laser-induced fluorescence. Recently, in some cases, it has been possible to study both photoproducts by this means.[15–17] However, the correlation between the scalar and vectorial measurements is only rarely addressed. For example, very few experimental studies have confronted the issue[18] of product rotational alignment and its importance in converting raw intensities in excitation spectra to populations.[19–21]

A powerful experimental approach that is capable of simultaneously measuring all the desired fragment scalar and vectorial properties is the one based on Doppler and polarization spectroscopy. We recently reported[22] the preliminary results of such a study on the OH fragment generated by the photolysis of *trans*-HONO at 369 nm:

$$\mathrm{HONO}(\tilde{X}) + h\nu \rightarrow \mathrm{HONO}(\tilde{A}) \rightarrow \mathrm{OH}(X\,^2\Pi) + \mathrm{NO}(X\,^2\Pi). \quad (1)$$

The lowest energy electronic transition in HONO (300–390 nm) has been previously ascribed to the $\tilde{A}\,^1A''$–$\tilde{X}\,^1A'$

band system.[23] It is now thought[24] to involve the excitation of a nonbonding electron on the terminal oxygen to an antibonding π^* orbital associated predominantly with the $-N=O$ chromophore, whereas a previous MO calculation[25] had assigned it to the promotion of a nonbonding electron on the N atom. Some of the $\tilde{A}$ state properties of the *trans* isomer are directly deducible from its $\tilde{A}$–$\tilde{X}$ absorption spectrum. For example, the only internal coordinate that undergoes an appreciable change upon electronic excitation is the N = O bond length since the spectrum mainly consists of a progression (2_o^n) of bands associated with the predominantly terminal NO stretching vibration (for convenience, we collect the HONO normal modes in Table I). In addition, the bands are diffuse, showing no discernible rotational structure.[23] The widths of the vibronic features imply an excited state lifetime $\sim 9\times 10^{-14}$ s, which is much shorter than the rotational period. HONO is thus a very attractive candidate for the observation of fragment motional (rotational and translational) anisotropy.

The fragmentation process (1) is closely related to the reaction

$$H(1s) + NO_2(\tilde{X}\,^2A_1) \rightarrow OH(X\,^2\Pi) + NO(X\,^2\Pi). \qquad (2)$$

One of the interesting aspects of the process (2) is that the OH $X\,^2\Pi\,\Lambda$ doublets are unequally populated.[26] The Λ doublets in a $^2\Pi$ state differ in the relative orientation of the π molecular orbital and the angular momentum **J**. In the classical (high J) limit, Π^+ refers to the π lobes being perpendicular to the internuclear axis and to **J** (i.e., in the plane of rotation), whereas the Π^- refers to the π orbital being parallel to **J** but perpendicular to the internuclear axis.[27] Quantum mechanically, the rotational symmetry of the Π^+ set of levels is the same as that of a Σ^+ state, whereas Π^- levels transform as those of a Σ^- state. In other words, the symmetry of Π^+ levels is given by $(-1)^N$, and those of Π^- by $(-1)^{N+1}$. Thus Π^+ and Π^- correspond to e and $f\Lambda$ doublets, respectively.[28] The two Λ doublets are easily probed experimentally because P, R lines connect Π^+ while Q lines connect Π^- for both spin-orbit components. The experimental Λ-doublet population ratio in the OH produced in process (2), serves as a sensitive probe for the geometry of the reactive trajectories.[26] This is explained in terms of a model first suggested in connection with the inverted Λ-doublet population in OH produced in the $H + H_2O$ reaction as being a possible source of OH interstellar 1665 MHz maser action.[27] The measured Π^+/Π^- population ratio of > 1.0 for the process (2) indicates that the reactive trajectories preferentially pass through the plane of the product OH rotation. Such population "anomalies" are also observed in photodissociation when the torque responsible for fragment rotation lies in a preferred plane.[17,19,29,30]

TABLE I. The normal modes of *trans*-HONO.[a]

Mode	Principal nuclear motion	Symmetry	ω/cm^{-1} $\tilde{X}$	$\tilde{A}$
ν_1	O–H stretch	a'	3590	
ν_2	N = 0 stretch	a'	1698	1139
ν_3	NOH bend	a'	1263	
ν_4	O–N stretch	a'	793	[b]
ν_5	ONO bend	a'	598	
ν_6	O–H torsion	a''	544	

[a] The vibrational frequencies are from Ref. 23.
[b] $\nu_4' \sim$ the fragmentation coordinate.

In our recent preliminary report[22] on the process (1), we presented results on the energy disposed into the OH fragment following excitation to the $\tilde{A}\,^1A''\,2^1$ level of HONO. Motional anisotropy was reported and briefly analyzed. The OH was found to be rotationally and vibrationally cold, and translationally hot ($\sim$0.5 eV). In addition, the $X\,^2\Pi$ spin-orbit components ($^2\Pi_{1/2}$ and $^2\Pi_{3/2}$) were found to be not in equilibrium. The gross features were compared with a simple impulse model[31] for photodissociation. One of the unsettled questions concerned the total amount of energy E_a available for distribution among the products. In the absence of any experimental proof to the contrary, E_a used in the impulse calculation included the quantum of energy initially deposited in the predominantly terminal NO stretching vibration ν_2 of the parent. It was thought that the validity of this vibrationally nonadiabatic assumption should be verifiable through experiments involving fragmentation via the higher members of the 2^n progression in the HONO $\tilde{A}$ state. Such measurements are relevant, e.g., in connection with the currently widely debated topic of intramolecular vibrational energy transfer in isolated molecules.[32] Such a process in HONO may be regarded as being an "internal $V \rightarrow T$" event, which may be thought of as arising from anharmonic coupling between the terminal NO stretch ν_2 and the fragment recoil coordinate ($\sim \nu_4$, the central ON stretch).

The results of such experiments are reported in this paper. *Trans*-HONO is photolyzed at wavelengths (354.7 and 341.8 nm) corresponding to the 2_0^2 and 2_0^3 bands. A detailed analysis is presented of the OH fragment motional anisotropy and energy distribution in all the degrees of freedom. Possible mechanisms for the production of OH vibration, rotation, motional anisotropy and fine-structure populations are discussed and compared with experiment. The NO fragment is not probed in our experiments because HONO coexists with NO and NO_2 (which is readily photolyzed to NO). Consequently, we merely theorize on its energy content. Next, experimental evidence is presented which unambiguously assigns the A'' symmetry to the HONO $\tilde{A}$ state. Finally, we discuss the nature of the $\tilde{A}$ state dissociation/predissociation and speculate on the qualitative features of the upper state surface.

II. EXPERIMENTAL

The basic experimental setup consists of a chamber through which the HONO photolysis and OH probe beams are counterpropogated. Three photolysis wavelengths have been used. Earlier experiments[22] involved photolysis at 368.9 nm, generated by Raman shifting in H_2 the second harmonic of a Nd:YAG laser. The present experiments involve excitation within the 2_0^2 and 2_0^3 bands of HONO. The wavelength (354.7 nm) for the first of these is obtained by frequency tripling the fundamental output of the Nd:YAG laser, while Stokes Raman shifting of the fourth harmonic of this laser generates 341.8 nm which is used to pump the 2_0^3 transition. The OH is probed by exciting the A–X (1,0) band

(281–285 nm) and monitoring the (1,1) emission (310–330 nm). For this purpose, a frequency-doubled dye laser (Molectron DL II) is used and fired approximately 30 ns after the photolysis laser pulse. The internal state distribution and the alignment are measured with a bandwidth of $\sim 1.2\ \mathrm{cm}^{-1}$. A high degree of polarization of the photolysis and probe beams is ensured by passing them through Rochon polarizers. For photofragment Doppler spectroscopy experiments, a bandwidth of $\sim 0.12\ \mathrm{cm}^{-1}$ is employed. A pressure-tuned intracavity air-spaced etalon is used in the dye laser for this purpose. The radiation density of the probe beam is well below the saturation limit, as shown by an experimental study of the probe power dependence of the OH line intensities, as well as by a calculation of the saturation effect using a crude (kinetic) model.[33]

Nitrous acid is prepared[34] by mixing H_2O vapor, NO_2, and NO in the ratio 1:2:1 to establish the surface-catalyzed equilibrium:

$$H_2O + NO_2 + NO \rightleftarrows 2HONO. \tag{3}$$

About 25 mTorr of this mixture is slowly flowed through the photolysis chamber.

For comparison, the excitation spectrum of thermalized (300 K) OH is also recorded. For this purpose, OH is generated by the $H + NO_2 \rightarrow OH + NO$ reaction (also at ~ 25 mTorr) and then allowed to collisionally equilibrate.

III. POPULATION DISTRIBUTION AND ALIGNMENT OF THE OH PHOTOFRAGMENT

The absence of hot bands in the excitation spectrum establishes that the OH fragment is vibrationally cold. The rotational distribution in the vibrationless ($v = 0$) level is probed through the A–X (1,0) band. Figure 1(a) shows an excitation spectrum of this band for the fragment resulting from the dissociation of the HONO $\tilde{A}\ 2^3$ level ($\lambda_{ex} = 342$ nm). For comparison, Fig. 1(b) displays the spectrum of thermalized (300 K) OH. The first conclusion that can be readily drawn is that the photofragment is also rotationally cold ($N'' \leqslant 7$). The most striking aspect in which the fragment spectrum differs from that of 300 K OH is that the R_2 branch is abnormally stronger than P_1. This implies that the $F_2(J = N - 1/2)$ spin-orbit component ($X\,^2\Pi_{1/2}$) is more highly populated than the F_1 ($J = N + 1/2$) component ($X\,^2\Pi_{3/2}$) in the OH photofragment.

The internal state distributions are, however, not accurately deducible directly from the raw experimental line intensities due to the alignment of the fragment. This is illustrated for the fragmentation of the 2^2 level of the HONO $\tilde{A}$ state ($\lambda_{ex} = 355$ nm) in Fig. 2 where we show the OH excitation spectra with two different orientations of the photolysis and analyzing-probe beam electric vectors, denoted by $\hat{\epsilon}_p$ and $\hat{\epsilon}_a$. In both cases, the photolysis and probe beams are counterpropagated while the fluorescence is detected at right angles to these by a photomultiplier which accepts all polarizations. However, as shown in the insets to Fig. 2, in one case [Figs. 2(a)], $\hat{\epsilon}_p \perp \hat{\epsilon}_a$ and the detection is along $\hat{\epsilon}_a$, while in the second configuration [Fig. 2(b)], $\hat{\epsilon}_p \| \hat{\epsilon}_a$ with the same detection direction. In the limit of fast fragmentation in the molecular plane, the first experimental geometry [Fig.

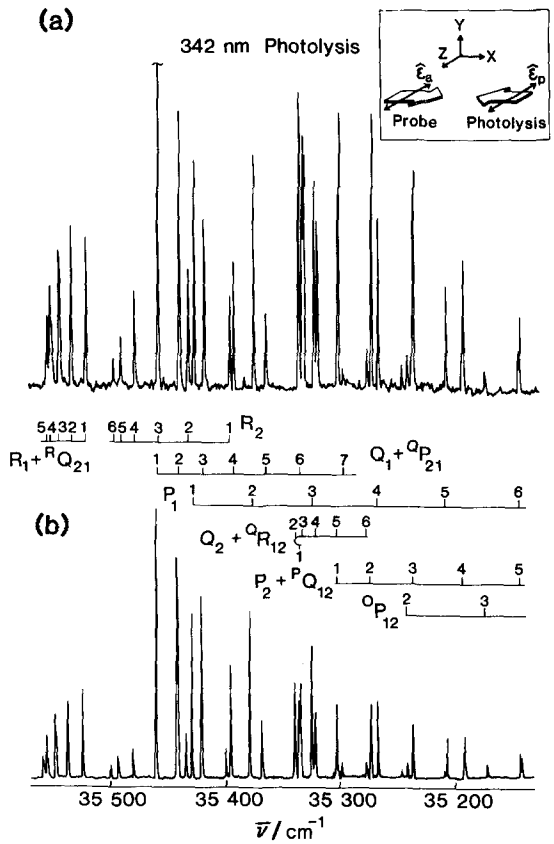

FIG. 1. A comparison of the (unnormalized) excitation spectra of (a) OH fragment generated by the 342 nm photolysis of HONO, and (b) thermalized (300 K) OH. The inset shows the experimental photolysis/probe geometry: the two beams, polarized along the Z axis are counterpropagated along the X axis. The fluorescence is detected along the Z axis by a photomultiplier which accepts *all* polarizations equally.

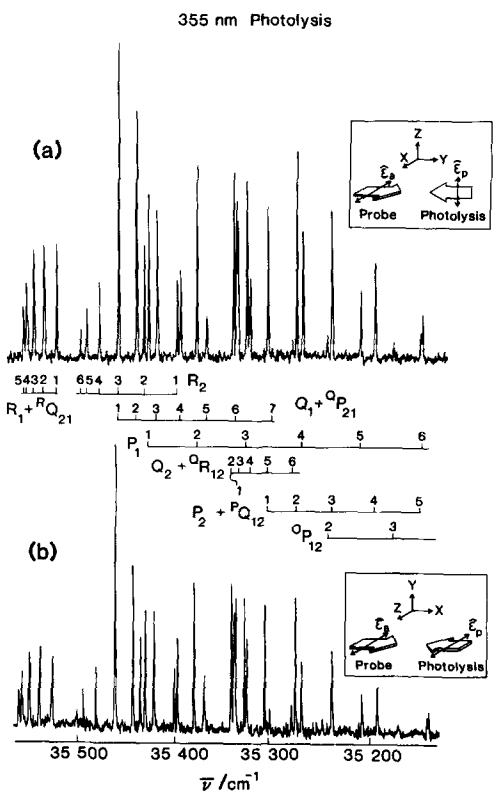

FIG. 2. Excitation spectra (unnormalized) of OH generated by HONO photolysis at 355 nm, with (a) $\hat{\epsilon}_p \perp \hat{\epsilon}_a$, and (b) $\hat{\epsilon}_p \| \hat{\epsilon}_a$. The fluorescence is detected in the same direction as in Fig. 1.

2(a)] favors the detection of P and R transitions at the expense of the Q branches. This is, of course, a direct consequence of the facts that the HONO $\tilde{A}$–$\tilde{X}$ transition moment is perpendicular to the molecular plane, so that $\hat{\epsilon}_p \perp \mathbf{J}_{OH}$ in the classical (high J) limit. Thus the probed transition moment for the P and R branches is in the plane of OH rotation while for the Q lines it lies along $\mathbf{J}_{OH}$. The reverse is true for the second experimental geometry [Fig. 2(b)]. It is thus clear that one has to deconvolute the effects of $\mathbf{J}_{OH}$ alignment to deduce accurate product populations. For this purpose, we rely on the treatment of Greene and Zare,[18] hereafter referred to as GZ. The portions essential to the present analysis are summarized below.

A. Fragment alignment

The treatment of GZ is applicable to any system with an axis of cylindrical symmetry, which is defined in the present experiments by the direction of $\hat{\epsilon}_p$ (the Z axis in Fig. 2). The effect of fragment alignment on a fluorescence intensity is given by

$$I = \mathrm{CS} \sum_{k_d,k_a,k} \mathscr{A}_0^{(k)} \epsilon(k_d,k_a,k,0;\Omega)\omega(k_d,k_a,k;J_i,J_e,J_f). \quad (4)$$

Here J_i, J_e, J_f are the rotational quantum numbers of the initial, excited, and final states in an excitation, emission cycle. The indices k_a, k_d refer to the multipole moments associated with the absorbed and detected photons, and k refers to the overall resonance fluorescence process. In general for an electric dipole absorption, such as OH A–X, these take the values $k_a = 0,2$; $k_d = 0,2$; $k = 0,2,4$. The factor C contains the population in the probed level i, and S is the product of the $e \leftarrow i$ and $e \rightarrow f$ line strengths. The product $\mathbf{J}_{OH}$ alignment is described in terms of the factors $\mathscr{A}_0^{(k)}$, where $\mathscr{A}_0^{(0)}$, $\mathscr{A}_0^{(2)}$, and $\mathscr{A}_0^{(4)}$ are, respectively, the initial state expectation values of the monopole, quadrupole, and hexadecapole combinations of the total angular momentum operator $\mathbf{J}$. For a photofragment generated by a dipole transition in the parent $\mathscr{A}_0^{(4)} = 0$ and $\mathscr{A}_0^{(2)}$ lies between the limits of -1 and 0.8 in the high J limit. The values of $\mathscr{A}_0^{(2)} > 0$ and $\mathscr{A}_0^{(2)} < 0$ correspond, respectively, to the cases of preferential population of the Zeeman levels with $|M_{J_i}| \sim J_i$ and that of $|M_{J_i}| \sim 0$. These, of course, correlate with the situations of $\mathbf{J}_i \| Z$ and $\mathbf{J}_i \perp Z$, respectively. Thus, a qualitative idea of the photofragment $\mathbf{J}$ alignment can be readily gained through relative (P,R) vs Q intensities in the experimental geometries shown in Figs. 2(a) and 2(b).

The geometrical factors $\epsilon(k_d,k_a,k,0;\Omega)$ in Eq. (4) refer to the polarization of the photolysis and probe beams, and to the polarization bias of the detection optics. The general equations for these polarization factors are given in GZ. The molecule-dependent part ω is a function of the quantum numbers J_i, J_e, J_f and the indices k_d, k_a, and k. It is most conveniently expressed as

$$\omega(k_d,k_a,k;J_i,J_e,J_f) = N_{k_d,k_a,k}\gamma_{k_dk_ak}(J_i,J_e,J_f)t_{ie}(J_i,J_e)t_{ef}(J_e,J_f). \quad (5)$$

Here the terms t_{ie} and t_{ef} serve to classify the transitions in the absorption and emission cycles respectively, and are given by

$$t_{ie} = 1 \text{ and } -2 \text{ for } (P\uparrow \text{ or } R\uparrow) \text{ and } Q\uparrow \text{ excitations,}$$

and

$$t_{ef} = 1 \text{ and } -2 \text{ for } (P\downarrow \text{ or } R\downarrow) \text{ and } Q\downarrow \text{ emissions,}$$

respectively.

In this form the coefficients $\gamma_{k_dk_ak}$ take simple values at high J independent of the absorption and emission branches. The formulas for calculating the various terms in Eqs. (4) and (5) for any arbitrary photolysis-probe-detection geometry are given by GZ. In our experiments we detect undispersed fluorescence, so that the polarization factors ω need to be summed over all the emission branches with appropriate weights corresponding to the OH line strengths.[35]

The fragment $\mathbf{J}$ alignment, as defined in Eq. (4), is somewhat complicated by the presence of hyperfine structure due to the proton nuclear spin ($I = 1/2$). The effective alignment is reduced due to the precession of $\mathbf{J}$ around $\mathbf{F}$, which is the total angular momentum inclusive of the nuclear spin angular momentum $\mathbf{I}$. As a result, the alignment factor is reduced, both in the initial state i and in the excited state e, especially at low J's. In the limiting cases of the ground state hyperfine precession time being shorter than the delay between fragment generation and detection, and the excited state lifetime being much longer than the excited state

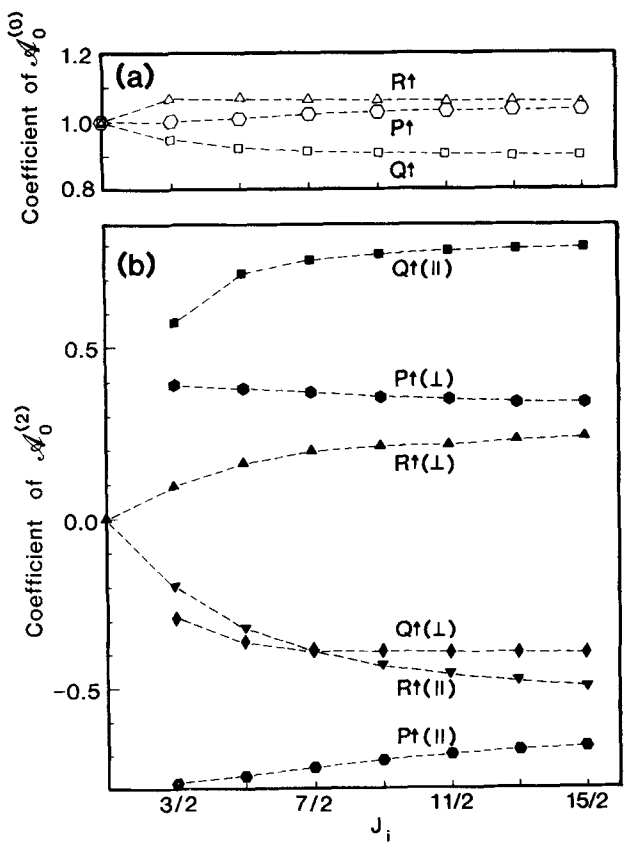

FIG. 3. Variation with J_i of the coefficients in Eq. (4) of (a) $\mathscr{A}_0^{(0)}$ and (b) $\mathscr{A}_0^{(2)}$. The distinction between the rotational transitions originating from the same J_i but different spin-orbit components F_1 and F_2 are negligible on this scale. The results in (a) refer to either photolysis/probe detection geometries, whereas in (b) (∥) represents $\hat{\epsilon}_a \| \hat{\epsilon}_p$ and (⊥) represents $\hat{\epsilon}_a \perp \hat{\epsilon}_p$.

precession period, the "dealignment" correction factors take especially simple forms, as given by GZ.

There is no experimental probe/detection geometry ("magic angle" configuration) which might permit one to directly invert the raw intensities in an excitation spectrum into fragment populations.[18] However, an analysis of the experimental geometries shown in the insets to Figs. 2(a) and 2(b) leads to a possible means of correcting for the alignment effects. We illustrate this in Fig. 3 where we plot, for the OH A–X (1,0) probed transitions, the coefficients of $\mathscr{A}_0^{(0)}$ and $\mathscr{A}_0^{(2)}$ in Eq. (4) as a function of J_i for each excitation branch (where we have summed over all the emission branches). Two conclusions are readily drawn from this figure: (1) For each excitation the coefficient of $\mathscr{A}_0^{(2)}$ for the geometrical arrangement shown in Fig. 2(a) is twice (in magnitude) that for the case shown in Fig. 2(b), but opposite in sign; and (2) for the $R_2(N=1)$ line, the coefficient of $\mathscr{A}_0^{(2)}$ is zero while that of $\mathscr{A}_0^{(0)}$ is almost unity. These observations afford a means for correcting for the effect of **J** alignment on line intensities. The procedure first involves normalizing the intensities of the fragment spectra for $\hat{\epsilon}_a \perp \hat{\epsilon}_p$ and $\hat{\epsilon}_a \| \hat{\epsilon}_p$ such that the $R_2(1)$ amplitudes are the same in the two cases. This is followed by taking, for each line, a weighted mean of the intensities in the two cases, where the weight for $\hat{\epsilon}_a \perp \hat{\epsilon}_p$ is twice that for $\hat{\epsilon}_a \| \hat{\epsilon}_p$. The OH internal state distributions evaluated in this paper are based on such an analysis.

B. Rotational distributions

The OH fragment internal state distribution for the 369 nm photolysis has been discussed previously.[22] Before presenting the results for the 355 nm and 342 nm photolyses, we mention a few important facts about the OH A–X (1,0) band which are relevant to our population analysis. We observe only low N ($\leqslant 6$ or 7) transitions. The problem of overlapping fine-structure doublets is thus especially bothersome at lower N's when evaluating lines in branches which are contaminated by associated satellites, particularly in cases where the separation between the main and satellite lines is comparable to the probe laser bandwidth. This difficulty is somewhat alleviated at higher N's in certain cases (e.g., $Q_2 + {}^PQ_{12}$) by the fact that the satellite line strengths are considerably less than those of the main line, and hence their contribution to the total "line" intensity may be neglected.

Figure 4 shows, for 369, 355, and 342 nm photolysis wavelengths, "Boltzmann" plots for the $X\,^2\Pi_{1/2}^+$ and $X\,^2\Pi_{3/2}^+$ sets of levels. These are obtained from the raw normalized intensities of the unblended P_1 and R_2 branches which have been corrected for alignment effects as summarized in Sec. III A.[36] The populations in $^2\Pi_{1/2}^+$ and $^2\Pi_{3/2}^+$ can be approximately characterized by "rotational temperatures": 385 ± 8 and 240 ± 16 K for 369 nm photolysis, 364 ± 20 and 253 ± 5 K for 355 nm photolysis, and 370 ± 10 and 269 ± 17 K for 342 nm photolysis. The plots of Fig. 4 serve the purpose of showing that (i) the two $^2\Pi$ spin-orbit F_1 and F_2 fine-structure components are not in equilibrium with each other although the members of each of these are reasonably well characterized by a "temperature"; (ii) the F_1/F_2 population ratios are N dependent; (iii) these ratios for $N=1$ are 1.81 for 369 nm photolysis, 1.66 at 355 nm, and 1.33 at 342 nm; and (iv) the rotational state distributions within the F_1 or F_2 components are not very sensitive to changes in the number of ν_2' quanta excited in the HONO $\tilde{A}$ state.

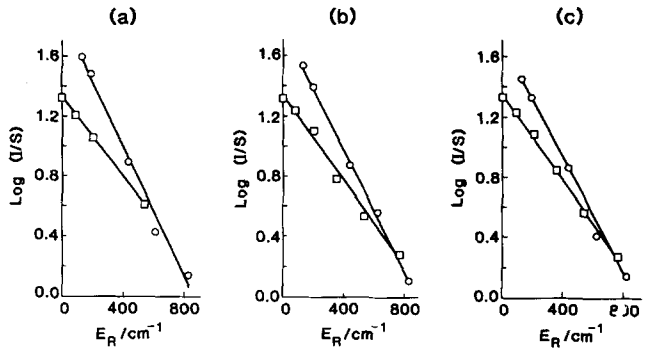

FIG. 4. Boltzmann plots for the $X\,^2\Pi_{1/2}^+$ (squares) and $X\,^2\Pi_{3/2}^+$ (circles) populations in OH produced by HONO photolysis at (a) 369 nm, (b) 355 nm, and (c) 342 nm. The line intensities used in these plots have been corrected for fragment alignment.

C. Λ-doublet populations

As mentioned in Sec. I, if the process (1) proceeds through a planar configuration, one expects (in the absence of exit-channel interactions) an "anomalous" Λ-doublet population ratio. Unambiguous evidence for such an effect in HONO $\tilde{A}$ state fragmentation is somewhat difficult to come by due to the facts that (a) many of the lines that need to be compared are overlapped; (b) as mentioned before, only low N transitions are observed and thus (because of satellite substructure) the $P_i(N)$ vs $Q_i(N)$ or $R_i(N)$ vs $Q_i(N)$ intensities ($i=1$ or 2) can be meaningfully compared only at higher N's where the satellites are weak enough to be neglected; and (c) many of the relevant lines are blended (see Figs. 1 and 2). In our previously reported experiments,[22] some of the crucial higher N lines were too weak for analysis. This problem has been overcome in the 355 and 342 nm photolysis experiments reported here.

We begin by comparing the $P_1(5)$ intensity with that of $Q_1(5)$. The former transition arises from the $X\,^2\Pi_{3/2}^+(N=5)$ level whereas the latter line originates from the $X\,^2\Pi_{3/2}^-(N=5)$. Even though the $Q_1(5)$ line is contaminated by its satellite $^QP_{21}(5)$, we neglect the latter's contribution on the grounds that its line strength is 9.4 times smaller than that of the main line and that their relative separation is relatively large (1.1 cm^{-1}). In the 355 nm-generated photoproduct, the $P_1(5)$ and $Q_1(5)$ alignment-corrected intensities are in the ra-

TABLE II. The OH photofragment $X\,^2\Pi_\Omega$ Λ-doublet population ratios.

		$[\Pi^+]/[\Pi^-]$ population ratio		
Ω	N	355 nm photolysis	342 nm photolysis	Calculated[a]
1/2	2	<1.58	<1.70	1.06
1/2	4	1.93 ± 0.15	2.00 ± 0.10	1.50
1/2	6	1.91 ± 0.30	2.13 ± 0.30	2.08
3/2	5	2.20 ± 0.30	2.24 ± 0.30	2.65

[a] From Eq. (19).

tio 1:0.77, whereas their line strengths are in the ratio 1:1.76. This implies that the $^2\Pi^+(5)/^2\Pi^-(5)$ population ratio is anomalously large by a factor of 2.2 ± 0.3. A similar treatment of $R_2(6)$ vs $Q_2(6)$, $R_2(4)$ vs $Q_2(4)$, and $R_2(2)$ vs $Q_2(2)$ intensities also shows the same type of anomaly. The results are collected in Table II and establish beyond doubt that the $^2\Pi^+$ levels are populated in preference to the $^2\Pi^-$ levels. In addition, the magnitude of this anomaly seems to be smaller at lower N. We return to this point in Sec. V.

D. Determination of the alignment parameter $\mathscr{A}_0^{(2)}(J)$

As is evident from Fig. 3, the R line intensities are relatively insensitive to the experimental photolysis/probe geometry, and thus the R intensities are not a very sensitive probe for the alignment effects. The P branches are somewhat more sensitive. The Q branches are the most sensitive, but tend to be more overlapped than the P branches. Thus the $P_1(N)$ intensities form the basis for estimating $\mathscr{A}_0^{(2)}$, especially at lower N's. $\mathscr{A}_0^{(2)}$ is then extracted from the ratios of line intensities in the two experimental polarization geometries, normalized as discussed before. The values of $\mathscr{A}_0^{(2)}(J)$, shown graphically in Fig. 5, range from 0.1 for $N = 1$ to 0.3 for $N = 5$. That $\mathscr{A}_0^{(2)}(J)$ is positive is, of course, readily obvious from the P, R vs Q intensities in Figs. 3(a) and 3(b). The large error bars are a consequence of uncertainties in small differences between large numbers.

Another means of calculating $\mathscr{A}_0^{(2)}(J)$ is provided by intensities of main and satellite lines originating from the same lower level. Their relative intensities in a single polarization geometry directly yield the value of $\mathscr{A}_0^{(2)}(J)$. An example is shown in Fig. 6. The top section shows a very small portion of a narrow band excitation spectrum in the 35 146–35 141 cm^{-1} region recorded with $\hat{\epsilon}_p \| \hat{\epsilon}_a$, which enhances

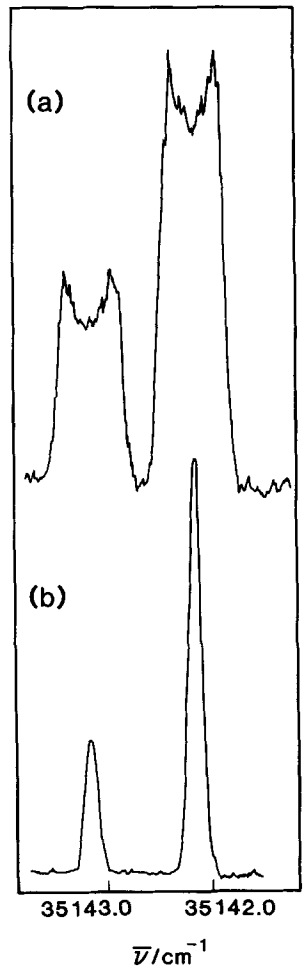

FIG. 6. Narrow-band excitation spectra in the 35 141–35 146 cm^{-1} region showing the $P_2(5)$ and $^PQ_{12}(5)$ lines of (a) the OH fragment produced by photolysis of HONO at 355 nm with $\hat{\epsilon}_p \| \hat{\epsilon}_a$ and (b) equilibrated (300 K) OH. The absence of saturation effects at the power density of the narrow-band probe laser is established by the fact that the relative intensities in the 300 K (isotropic) OH spectrum agree with those calculated with $\mathscr{A}_0^{(2)} = 0$.

the Q branch at the expense of the P and R branches. A discussion of the fragment line shapes observed here with a narrow-band probe is deferred to the next section. The only important aspect relevant here is the $P_2(5)$ vs $^PQ_{12}(5)$ intensity ratio. From these relative intensities and the values of the coefficients of $\mathscr{A}_0^{(0)}$ and $\mathscr{A}_0^{(2)}$, shown in Fig. 3, we deduce that $\mathscr{A}_0^{(2)}(J) = +0.33 \pm 0.05$ for $X\,^2\Pi_{3/2}^-(N = 5)$. The results of a similar treatment for $P_2(4)$ vs $Q_2(4)$ and $Q_1(3)$ vs $^QP_{21}(3)$ intensities are incorporated in Fig. 5, along with the results obtained from the 342 nm-generated photofragment P_1 branch intensities. Although the calculated $\mathscr{A}_0^{(2)}(J)$ values are associated with rather large uncertainties, the trend towards higher values with increasing N seems to be real.

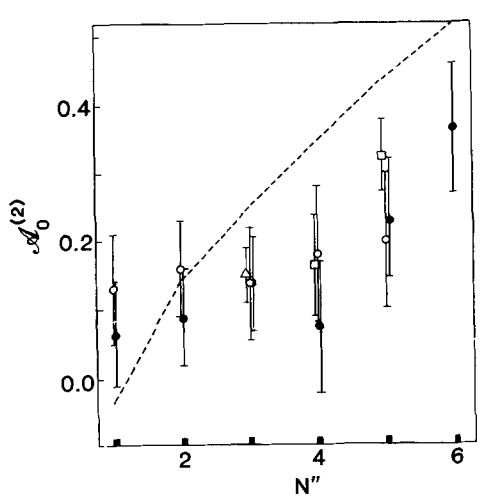

FIG. 5. The OH photofragment alignment parameter $\mathscr{A}_0^{(2)}(J)$ vs N''. The filled circles (●) refer to the 355 nm-generated fragment alignment in the $X\,^2\Pi_{3/2}^+$ levels, as derived from the P_1 branch intensities, while the open triangle (△) and open squares (□) refer, respectively, to these of the $X\,^2\Pi_{3/2}^-$ and $X\,^2\Pi_{1/2}^+$ levels, deduced from the $(Q_1, ^QP_{21})$ and $(P_2, ^PQ_{12})$ transitions (see the text). The open circles (○) represent the $\mathscr{A}_0^{(2)}(J)$ of the $X\,^2\Pi_{3/2}^+$ levels of the fragment obtained by 342 nm photolysis. The broken line is the calculated value of $\mathscr{A}_0^{(2)}(R = N'')$ assuming Gaussian distributions for the fragment rotation originating from in-plane and out-of-plane bends (see the text).

IV. PHOTOFRAGMENT DOPPLER PROFILES

Figure 6 shows a portion of the OH photofragment excitation spectrum recorded with a probe bandwidth of ~ 0.1 cm^{-1}. Also shown, for comparison, is the profile of thermalized (300 K) OH. The fragment profiles are characterized by their much larger widths (FWHM$\simeq$0.6 cm^{-1}), a central minimum, and by sharp edges at the extremes. The width is due to the Doppler effect resulting from the recoil of the fragments. The double-peaked shape, which we term a Doppler-split profile, indicates that there are more OH fragments moving with high velocity components than those with low velocity components along the probe laser direction. Since this direction (X axis, Fig. 1) is perpendicular to $\hat{\epsilon}_p$

(the Z axis), the observed line shape corresponds to an anisotropic OH translation predominantly in the XY plane.

In general, the fragment velocity vector $\mathbf{V}_{OH}$ is correlated with the fragment angular momentum vector $\mathbf{J}_{OH}$. Consequently, it is conceivable that the line shape function contains contributions from both the fragment Zeeman (M_J) anisotropy and the fragment translational ($\mathbf{V}_{OH}$) anisotropy, causing the line shape to be probe-polarization-dependent across its profile. However, there are situations where this polarization dependence is expected to be small. For example, this should be the case when (a) $\mathscr{A}_0^{(2)}$ is small, or (b) when the parent molecule rotation makes an insignificant contribution to fragment rotation, so that $\mathbf{J}_{OH}$ makes a constant angle with respect to $\mathbf{V}_{OH}$ for all recoil velocities. The latter is expected to be valid in the present case as will be discussed in Sec. V. Experimentally, this is established by, e.g., the fact that the same profiles are observed with $\hat{\epsilon}_a \perp \hat{\epsilon}_p$ and $\hat{\epsilon}_a \| \hat{\epsilon}_p$ for all members of the P_1 branch ($N = 1$–6). In what follows, we use the experimental $P_1(1)$ profile to determine the OH fragment anisotropic recoil velocity.

The center of mass fragment angular distribution for a single fragment recoil velocity and for a linearly polarized parent photolysis is given by

$$W(\theta) = \frac{1}{4\pi}\{1 + \beta P_2(\cos\theta)\}, \tag{6}$$

where $P_2(x) = (3x^2 - 1)/2$ and θ is the angle between the fragment recoil direction and $\hat{\epsilon}_p$. The anisotropy parameter β lies between $+2$ and -1, corresponding respectively to the limiting cases of recoil along and perpendicular to the parent molecule transition moment. The corresponding fragment Doppler profile is given by[3,22,37]

$$\mathscr{S}(\Delta\bar{\nu}_0) = \frac{1}{\Delta\bar{\nu}_D}\{1 + \beta P_2(\cos\theta) P_2(\Delta\bar{\nu}_0/\Delta\bar{\nu}_D)\}, \tag{7}$$

where $\Delta\bar{\nu}_D = \bar{\nu}_0 V/c$ is the Doppler shift and $\Delta\bar{\nu}_0$ is the displacement from the line center $\bar{\nu}_0$. For our detection geometry, $\theta = \pi/2$. For the case of the parent transition moment being perpendicular to the bond that breaks and in the limit of fast fragmentation, as in the case at hand, the above equation reduces to

$$\mathscr{S}(\Delta\bar{\nu}_0) = \frac{1}{\Delta\bar{\nu}_D}\left\{1 - \frac{1}{2}\beta P_2\left(\frac{\Delta\bar{\nu}_0}{\Delta\bar{\nu}_D}\right)\right\}, \tag{8}$$

where $\beta = -1$.

An actual simulation of a Doppler profile should allow for the spread of fragment recoil velocities, the finite probe laser bandwidth and the transformation from the center of mass to the laboratory frame. The latter is particularly trivial in the present "bulb" experiment, since the parent motion is isotropic. This requires a convolution of the center of mass Doppler profile with the 300 K thermal Gaussian parent distribution. The laser profile is determined here from the thermal OH line shapes (FWHM $= 0.157\ \mathrm{cm}^{-1}$). Deconvolution with a 300 K thermal OH Gaussian profile (FWHM $= 0.105\ \mathrm{cm}^{-1}$) gives a time-averaged Gaussian laser profile with a FWHM of $0.116\ \mathrm{cm}^{-1}$. The combination of this with the parent motion gives an overall Gaussian convolution function with a FWHM $= 0.132\ \mathrm{cm}^{-1}$.

We first consider the limiting case of $\beta = -1$ and a single recoil velocity.[38] Best agreement between the observed and simulated convoluted linewidth is obtained with $2\Delta\bar{\nu}_D = 0.61\ \mathrm{cm}^{-1}$. This was in fact the simulation reported earlier[22] for the 369 nm photolysis-generated OH. However, the agreement of the central dip/peak height ratio between the observed (0.20–0.22) and calculated (0.27) profiles is not perfect. A better agreement between the two is obtained with $\beta = -0.8$ and $2\Delta\bar{\nu}_D = 0.59\ \mathrm{cm}^{-1}$. This is illustrated in Fig. 7 and compared with the experimental $P_1(1)$ line shapes for the 369, 355, and 342 nm-generated fragments.

The simulation presented in Fig. 7 is based on the assumption of a delta-function distribution of fragment velocities and $\beta = -0.8$. The contrast of the central dip can however also be generated by $\beta = -1$ and a distribution of velocities $f(V)$. In other words, so far as the central dip is concerned, β and $f(V)$ are correlated. Fortunately, this correlation can be somewhat broken when the wings of the Doppler profile are considered. We illustrate this point with a Gaussian $f(V)$ distribution with, say, a 30% spread. Although the simulation with $\beta = -1$ produces the correct central contrast, the wings extend significantly more from the center than is observed and have a lower slope at the extremes. The simulation shown in Fig. 7 on the other hand shows a steep rise at the extremes, as experimentally observed. Thus, if a distribution $f(V)$ is responsible for the lowering of the central contrast, it must have a sharp cutoff on the high velocity side. In any case, the point we wish to make

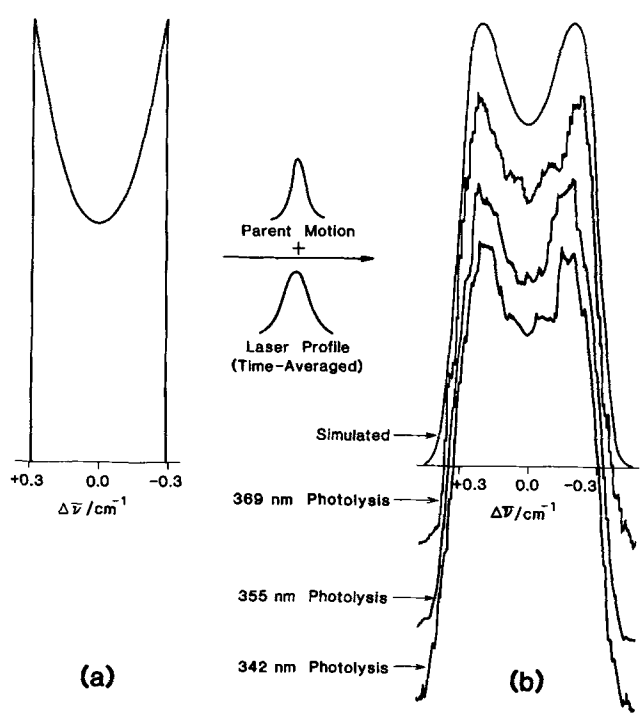

FIG. 7. The Doppler line shape (a) calculated from $\mathscr{S}(\Delta\bar{\nu}_0)$ using Eq. (6) with $\beta = -0.8$ and $2\Delta\bar{\nu}_D = 0.59\ \mathrm{cm}^{-1}$, and (b) obtained by convoluting ($\Delta\bar{\nu}_0$) with a 300 K thermal parent motion (FWHM $= 0.063\ \mathrm{cm}^{-1}$) and a time-averaged Gaussian laser profile (FWHM $= 0.116\ \mathrm{cm}^{-1}$), deduced from the thermalized OH line shape. The simulation is based on the assumption of a single fragment recoil velocity (see the text). Shown below the simulated profile in (b) are the experimental $P_1(1)$ line shapes for the OH photoproduct generated at 369, 355, and 342 nm.

here is that β is close to the limiting value of -1 ($-0.8 \geqslant \beta \geqslant -1.0$).

Either calculation leads to $\Delta\bar{\nu}_D = 0.295 \pm 0.010\ \mathrm{cm}^{-1}$ for the (mean) Doppler shift, corresponding to a (mean) recoil velocity of 2.50 km/s^{-1} or a translational energy of 4491 cm^{-1} (0.55 eV).

The experimental profiles in Fig. 7 demonstrate that the Doppler shift is insensitive to the photolysis wavelength. In addition, it is also N independent as shown by the fact that the central contrast in the P_1 branch, e.g., is constant for the range (1–6) of N studied. The consequences of these observations are discussed in the next section.

V. MECHANISMS FOR THE GENERATION OF OH FRAGMENT INTERNAL STATES AND TRANSLATION

The Franck–Condon (FC) principle readily offers an explanation for the observation that the OH photoproduct is vibrationally cold. The OH bond length in the parent is $\sim$0.98 Å, and is 0.97 Å in the fragment. This implies that the FC factors for the decomposition of HONO ($\tilde{A}, v_1 = 0$) to OH (X,v) are diagonal, i.e., the fragmentation predominantly results in the vibrationless product.

There are many possible sources for the OH fragment rotation. The first obvious consideration is parent rotation. Since the HONO excited state fragments on a time scale much faster than the rotational period, the OH rotation due to this mechanism must correlate with the parent *ground* state rotation. Approximate calculations based on the parent ground state rotational constants show that, if the OH angular velocity in HONO is mapped onto the fragment, then this mechanism amounts to only $\sim$13 cm^{-1} of OH rotational energy (originating predominantly from the rotation around the parent a axis, which is slightly inclined to the central O–N bond). This contribution is thus too small to account for the present observations.

Another possibility involves an impulse associated with the fragmentation, as described previously.[22] In this model,[31] the OH rotation arises from the torque exerted on the O atom by the impulse directed along the central O–N bond. This picture is valid only if the OH is regarded as a rigid unit, so that the H atom would respond to the impulse exerted on the O atom, thus resulting in the rotation of the OH fragment. Calculations based on the assumption that it is the electronic energy ($\sim$9161 cm^{-1}) in excess of that corresponding to the separated OH ($X\,^2\Pi$) and NO ($X\,^2\Pi$) components that is "available" for partitioning,[39] imply that 250 cm^{-1} should appear as OH rotation with about 4310 cm^{-1} disposed into translation. Furthermore, this model implies a relatively sharply peaked non-Boltzmann rotational distribution and also a partitioning of the available energy into OH translation and rotation. Since this is not experimentally observed, we conclude that the impulse model cannot account for the observed rotational energy content of the OH fragment. This is presumably because the O–H bond is not rigid enough for the H atom to respond to the impulse exerted on the O atom by the O–N bond cleavage. The energy available to OH must then be presumably channeled almost exclusively into translation. In fact, if all the impulse-contributed energy is asumed to go into OH recoil, the value E_T (OH) = 4559 cm^{-1} is close to the experimental value of 4491 $\pm$ 300 cm^{-1}. If this is true, the origin of OH fragment rotation lies elsewhere.

We propose that the OH product rotation originates from the angle bending vibrations in the parent. As shown in Table I, two such vibrations exist in HONO: the in-plane H–O–N bending vibration ν_3 and the out-of-plane torsion ν_6, with the frequencies of 1263 and 544 cm^{-1} in the ground state. The corresponding excited state values are not known experimentally. However, since the HONO excited state lifetime is long enough for a well defined vibrational (ν_2') structure to be developed, it is the excited state ν_3' and ν_6' frequencies that must enter any model calculation. Since these are unknown, we are forced to make the highly questionable assumption that ν_3 and ν_6 decrease by the same amount as the frequency of the only known upper state vibration ν_2 changes upon electronic excitation. In this manner, we "guesstimate" $\omega_3' \simeq 846$ cm^{-1} and $\omega_6' \simeq 364$ cm^{-1}.

Such a model has been considered previously by Freed, Morse, and Band[7] in connection with the photodissociation of triatomic systems, where the Gaussian distribution of parent bending vibrational momentum is transformed into a Gaussian diatomic fragment rotational distribution. For a two-dimensional isotropic oscillator the overall distribution is thus characterized by a "rotational temperature." We adopt Freed *et al.* general approach and, for the in-plane motion, we regard the terminal O atom as a mere "spectator." For a nonrotating parent, the ν_3'-induced rotational energy is given by

$$\langle E_R \rangle_{\mathrm{OH}}^{\parallel} = \frac{\omega_3'}{4} \frac{m_{\mathrm{H}} m_{\mathrm{O}} \{ r_{\mathrm{ON}}/m_{\mathrm{H}} - [r_{\mathrm{HO}} \cos\phi_1 - r_{\mathrm{ON}}]/m_{\mathrm{O}} \}^2}{m_{\mathrm{HO}} \{ r_{\mathrm{ON}}^2/m_{\mathrm{H}} + [r_{\mathrm{HO}}^2 - 2 r_{\mathrm{HO}} r_{\mathrm{ON}} \cos\phi_1 + r_{\mathrm{ON}}^2]/m_{\mathrm{O}} + r_{\mathrm{HO}}^2/m_{\mathrm{N}} \}}, \tag{9}$$

where ϕ_1 is the H–O–N angle. This gives

$$\langle E_R \rangle_{\mathrm{OH}}^{\parallel} = 205\ \mathrm{cm}^{-1} \tag{10}$$

for the in-plane fragment rotation. The out-of-plane torsional vibration ν_6' generates product angular momentum in a plane perpendicular to the molecular frame. This contribution is given by

$$\langle E_R \rangle_{\mathrm{OH}}^{\perp} = \frac{\omega_6' m_{\mathrm{H}} m_{\mathrm{O}} \{ r_{\mathrm{ON}} \sin\phi_2/m_{\mathrm{H}} + [r_{\mathrm{HO}} \sin(\phi_1 - \phi_2) + r_{\mathrm{ON}} \sin\phi_2]/m_{\mathrm{O}} \}^2 r_{\mathrm{NO}}^2}{4 m_{\mathrm{HO}} \{ [r_{\mathrm{ON}} r_{\mathrm{NO}} \sin\phi_2]^2/m_{\mathrm{H}} + r_{\mathrm{NO}}^2 [r_{\mathrm{HO}} \sin(\phi_1 - \phi_2) + r_{\mathrm{ON}} \sin\phi_2]^2/m_{\mathrm{O}} + r_{\mathrm{HO}}^2 [r_{\mathrm{ON}} \sin\phi_1 - r_{\mathrm{NO}} \sin(\phi_1 - \phi_2)]^2/m_{\mathrm{N}} + [r_{\mathrm{HO}} r_{\mathrm{ON}} \sin\phi_1]^2/m_{\mathrm{O}} \}}, \tag{11}$$

where ϕ_2 is the O–N–O angle. This yields

$$\langle E_R \rangle_{\rm OH}^{\perp} = 88\ {\rm cm}^{-1}. \tag{12}$$

Brief derivations of Eqs. (9) and (11) are presented in the Appendix.

The above picture indicates that the higher OH product rotation arises predominantly from the in-plane parent vibration ν_6'. On the other hand, the lower fragment rotation originates from both ν_3' and ν_6' and thus should be more isotropic. In other words, the alignment of OH nuclear rotation (**R**) should be smaller for lower N values and increase with N.

We calculate $\mathscr{A}_0^{(2)}$ classically by assuming Gaussian distributions[7] for the in-plane and out-of-plane components of **R**, denoted by $R_\parallel$ and $R_\perp$, respectively, where **R** must be perpendicular to the internuclear axis of the OH fragment. Let θ_R be the angle between **R** and the electric vector $\hat{\epsilon}_p$ of the photolysis beam (Fig. 8). Then the classical value of the alignment parameter for **R** may be written as

$$\mathscr{A}_0^{(2)}(R) = \frac{\frac{4}{5}\int_0^{2\pi} f_R(\theta_R) P_2(\cos\theta_R) d\theta_R}{\int_0^{2\pi} f_R(\theta_R) d\theta_R}, \tag{13}$$

where

$$f_R(\theta_R) = (\rho_\parallel \rho_\perp)^{1/2} \pi^{-1} R \exp[-\rho_\parallel R_\parallel^2 - \rho_\perp R_\perp{}^2] \tag{14}$$

describes the angular distribution of **R**. Here

$$R_\parallel = R\cos\theta_R, \tag{15a}$$

$$R_\perp = R\sin\theta_R, \tag{15b}$$

$$\rho_\parallel = \frac{B}{\langle E_R \rangle_{\rm OH}^{\parallel}} \frac{E'_{v_3}}{\omega_3'} \tag{15c}$$

and

$$\rho_\perp = \frac{B}{\langle E_R \rangle_{\rm OH}^{\perp}} \frac{E'_{v_6}}{\omega_6'}, \tag{15d}$$

where B is the rotational constant of the OH fragment and E'_{v_i} is the energy in the bending vibration ν_i. For a zero-point nondegenerate bend $E'_{v_i}/\omega_i' = 1/2$.

The vector **R** is the nuclear component of **N**, where **N** makes a projection Λ on the OH internuclear axis. Hence **N** is only perpendicular to the internuclear axis of OH at high N. We calculate the alignment parameter for **N** in a manner exactly analogous to Eq. (13):

$$\mathscr{A}_0^{(2)}(N) = \frac{\frac{4}{5}\int_0^{2\pi} f_N(\theta_N) P_2(\cos\theta_N) d\theta_N}{\int_0^{2\pi} f_N(\theta_N) d\theta_N}, \tag{16}$$

where $f_N(\theta_N)$ represents the angular distribution of **N** with respect to $\hat{\epsilon}_p$. We then approximate the angular distribution of **N** by

$$f_N(\theta_N) = (\rho_\parallel \rho_\perp)^{1/2} \pi^{-1} (N + \tfrac{1}{2}) \exp\{-[N(N+1) - \Lambda^2] \times [\rho_\parallel \cos^2\theta_N + \rho_\perp \sin^2\theta_N]\}, \tag{17}$$

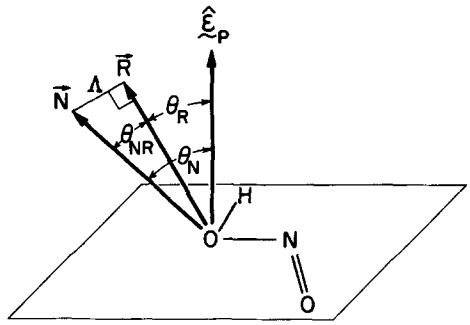

FIG. 8. Coordinates used in the calculation of the OH fragment rotational alignment. The rotational angular momentum **N** can be resolved into the nuclear rotational angular momentum **R** and a projection Λ of the electronic orbital angular momentum. **N** and **R** make the angles θ_N and θ_R with respect to the photolysis electric vector $\hat{\epsilon}_p$.

where

$$\cos^2\theta_N = \sin^2\theta_{NR}\cos^2\theta_R = \left[\frac{N(N+1) - \Lambda^2}{N(N+1)}\right]\cos^2\theta_R. \tag{18}$$

This semiclassical description is of course inaccurate at low N but should represent $\mathscr{A}_0^{(2)}(N)$ with increasing N. The values of $\mathscr{A}_0^{(2)}(N)$ calculated for $N = 1$–6 from Eqs. (16)–(18) are shown as a broken line in Fig. 5. They follow the trend of the experimental values which show increasing alignment with increasing rotation. The experimental values strictly refer to $\mathscr{A}_0^{(2)}(J)$. However, we defer converting the calculated $\mathscr{A}_0^{(2)}(N)$ to $\mathscr{A}_0^{(2)}(J)$ because the above semiclassical treatment does not warrant a more elaborate calculation involving the uncoupling of electron spin with increasing rotation [case(a)–case(b) intermediate behavior].

If the above mechanism for OH rotational excitation is correct, then it should also be reflected in the relative populations of the Π^+ and Π^- Λ-doublet components. The π orbital on the OH fragment is initially associated with the central O–N bond. Since the higher fragment rotation is thought to arise predominantly from the in-plane bending vibration (which is in a plane containing the OH fragment π orbital), one expects Π^+ rotational levels to be more highly populated than the corresponding Π^- levels at high N. This is indeed observed (see Table II).

To derive the OH rotational alignment from the Π^+:Π^- population ratio for a given rotational state, we must consider the orientation of the π lobe with respect to

TABLE III. "Observed" and calculated values of the orientation of the peak in the fragment π orbital charge distribution with respect to the plane of rotation (see the text).

		Angle between fragment π orbital and plane of rotation		
		"Observed"		Calculated
Ω	N	355 nm photolysis	342 nm photolysis	from Eqs. (19) and (22)
1/2	2	> 14°	> 9°	40°
1/2	4	21 ± 3°	20 ± 2°	29°
3/2	5	23 ± 3°	22 ± 3°	24°
1/2	6	12 ± 4°	20 ± 2°	18°

the plane of rotation as function of rotation. As first discussed by Gwinn *et al.*[27] the orientation of the π lobe is conveniently expressed in terms of $\Delta = \langle \cos^2\phi - \sin^2\phi \rangle$, where ϕ is the angle between the π lobe and the plane of rotation.[40] For the Π^+ component Δ varies from 0 at $J = 1/2$ to 0.5 at high J, whereas for the Π^- component Δ varies from 0 to -0.5. Suppose that the photodissociation dynamics are such that the plane of rotation of the OH fragment makes an angle θ with respect to the π lobe (assumed to be along the O–N bond of the HONO parent). As Fig. 8 shows, we may associate θ with θ_R. This nascent OH wave function must then be projected on to the true OH functions. Then the populations of the Π^+ and Π^- components, denoted by $[\Pi^\pm]$, are proportional to $\frac{1}{2} \pm \Delta\,(\cos^2\theta_R - \sin^2\theta_R)$, so that

$$\frac{[\Pi^+]}{[\Pi^-]} = \frac{1+2\Delta\delta}{1-2\Delta\delta}, \tag{19}$$

where

$$\begin{aligned}\delta &= \langle \cos^2\theta_R - \sin^2\theta_R \rangle \\ &= \int_0^{2\pi} f_R(\theta_R)(\cos^2\theta_R - \sin^2\theta_R)d\theta_R \Big/ \int_0^{2\pi} f_R(\theta_R)d\theta_R \\ &\simeq \int_0^{2\pi} f_N(\theta_N)(\cos^2\theta_N - \sin^2\theta_N)d\theta_N \Big/ \int_0^{2\pi} f_N(\theta_N)d\theta_N.\end{aligned} \tag{20}$$

In Table II we compare the $[\Pi^+]/[\Pi^-]$ ratio determined experimentally, with that calculated from Eqs. (19) and (20). The comparison is not perfect, but does show the correct sign and magnitude.

It may also be useful to consider the shape of the π lobe charge density. For $J = 1/2$, this quantity is cylindrically symmetric, while for $J > 1/2$, the electron charge density of the π lobe peaks at $\phi^\pm$ for the $\Pi^\pm$ component (see Fig. 9). It can be shown that

$$\phi^\pm = \cos^{-1}(\tfrac{1}{2} \pm |\Delta|)^{1/2}. \tag{21}$$

Recalling that the plane of rotation of the OH fragment makes an angle θ_R with respect to the π lobe, then the population of the $\Pi^\pm$ component is proportional to $\cos^2(\phi^\pm - \theta_R)$, i.e.,

$$\frac{[\Pi^+]}{[\Pi^-]} = \frac{\cos^2(\phi^+ - \theta_R)}{\cos^2(\phi^- - \theta_R)}. \tag{22}$$

We use Eq. (22) to deduce the angle θ_R for each J from the experimental Λ-doublet population ratios $[\Pi^+]/[\Pi^-]$ and the values of $\phi^\pm$ obtained from Eq. (21) using the known value of Δ for OH. The results are collected in Table III. Also included in Table III are the values obtained from Eqs. (19) and (22). The comparison with experimental values is not perfect but does show fair agreement.

All the available evidence is thus consistent with the conclusions that the HONO $\tilde{A}$ state is planar, the OH fragment rotation is derived predominantly from the angular momenta generated by the in-plane and out-of-plane vibrations ν_3' and ν_6' in the parent, and the energy available to the OH fragment due to the impulse associated with the central O–N bond cleavage is channeled mostly into translation.[41]

The relative F_2/F_1 populations, as mentioned previously, are not in equilibrium with rotational motion. In thermal OH, the absolute population of $F_2(N)$ is lower than that of $F_1(N)$ for two reasons: F_2 lies higher in energy by 126 cm^{-1} for $N = 1$, decreasing to 56 cm^{-1} for $N = 6$; and F_2 has a statistical weight of $2N$ compared with $2(N+1)$ for F_1. This statistical weight ratio is automatically taken into account in constructing a Boltzmann plot. The photofragment spectra show an $F_2(1)/F_1(1)$ absolute ratio ranging from 0.91 for 369 nm photolysis, 0.83 at 355 nm, and 0.67 for the 342 nm case. These correspond to statistically weighted ratios of 1.81, 1.66, and 1.33, respectively.

As shown previously, the product rotation and vibration can be understood in terms of Freed *et al.* generalized Franck–Condon theory of photofragmentation, which involves the use of a sudden approximation. We discuss the possibility that such a model explains the spin-orbit population distributions. Since the unstable parent state is a singlet, the spins of the odd electron on each of the fragments are presumed to be coupled (to yield a resultant singlet) even after the sudden cleavage of the parent ON bond. There is no preferred axis for each spin—merely the requirement that the two spin orientations be correlated. This implies that the nuclear rotation angular momentum of the recoiling OH be independent of the electron spin angular momentum. In the simplest sudden approximation, the random spin orientation is projected on to the OH case (b) quantum states. This, however, predicts a statistical $F_2(N)/F_1(N)$ population in spite of their energetic difference. Allowance for true case (a)/case (b) intermediate coupling enhances the F_2/F_1 ratio but only to the extent of a mere 4% for $N = 1$. Even though these departures from equilibrated spin and rotational populations are in the correct sense, the experimental anomaly is much more extreme than this, and, in addition, is also a function of the photolysis wavelength. Thus, we are led to seek other possible explanations.

Our observations indicate the presence of an interaction which is magnetic in origin since the fragment electron spin apparently has a preferred orientation with respect to the electron orbital angular momentum. Furthermore, this ef-

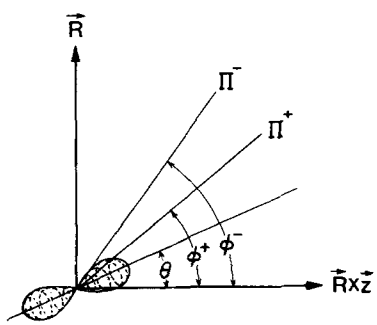

FIG. 9. The geometrical coordinates used in the calculation of the orientation of the π lobe in the OH fragment. Here **R** is the axis of nuclear rotation; **z** is along the internuclear axis and is perpendicular to the plane of the figure; **R**×**z** is in the plane of rotation; $\phi^\pm$ is the angle between **R**×**z** and the peak in the π lobe angular distribution for the $\Pi^\pm$ Λ doublets. In the photoproduct, due to the nature of the dynamics of fragment rotational excitation, the π lobe makes an angle θ with **R**×**z**, causing an unequal population of the Λ doublets.

fect changes as a function of the photolysis wavelength. Spin-orbit interaction of the initially prepared singlet with a nearby triplet state could provide the desired energy-dependent mechanism. Alternately, the F_2/F_1 populations may be the result of inelastic scattering between the recoiling fragments. This possibility is especially attractive here since the spin-orbit splittings in OH ($X\,^2\Pi_{\rm inv}$) and NO ($X\,^2\Pi_{\rm reg}$) are very similar in magnitude. The variations in the OH product spin-orbit distributions with ν_2' may be attributed to the different vibrational distributions of the NO fragment in each case.

If the OH,NO near-resonant inelastic scattering is indeed responsible for the OH photofragment nonequilibrium spin-orbit populations, this should also be reflected in the NO fragment F_2/F_1 populations. Unfortunately, since HONO coexists [see Eq. (3)] with NO and NO_2 (which is readily photolyzed to NO), we have not attempted to probe the NO fragment generated by HONO photolysis. However, indirect evidence in support of the above mechanism comes from recent experiments[42] on NO obtained by the photolysis of CH_3ONO, which is structurally similar to HONO and, fortunately, unlike HONO, is chemically stable. Since the unpaired electron on the OH $X\,^2\Pi$ free radical largely resides on the oxygen atom,[43] the replacement of the hydrogen atom by a methyl group changes the spin-orbit splitting only by a small amount.[44] We may therefore be justified in comparing the OH $^2\Pi_{1/2}/^2\Pi_{3/2}$ populations in HONO photolysis with that of NO from CH_3ONO.

The experiments of Lahmani *et al.*[42] on CH_3ONO photolysis show that, compared with thermal populations, the NO fragment $^2\Pi_{1/2}$ is more highly populated than $^2\Pi_{3/2}$. This is consistent with our hypothesis that the peculiar spin-orbit populations in the OH obtained from HONO photolysis might be due to OH $^2\Pi_{\rm inv}$, NO $^2\Pi_{\rm reg}$ inelastic scattering.[45]

VI. INFLUENCE OF PARENT ν_2 VIBRATION; ENERGY DISTRIBUTION IN THE NO FRAGMENT

The relative inactivity of the parent ν_2 vibration, so far as the OH fragment energy is concerned, is intriguing. Classically, the effect of a given parent normal mode on fragmentation may be visualized in terms of the variations in the internal coordinates evolving into the trajectories of the recoiling fragments. The influential factors might be (a) the anharmonic coupling between this and other modes, especially the one to which the fragmentation coordinate correlates; and (b) the "duration" of dissociation, which ideally should be long enough to permit the development of the desirable phase relationship between the optically prepared vibrational displacement and the motion along the dissociation coordinate. The implication of the present experimental findings is that the anharmonic coupling between the zero-order normal modes ν_2' and ν_4' is not large enough to be effective in transferring the terminal –N = O stretching vibrational (ν_2') momentum to the fragmentation coordinate ($\sim\nu_4'$) during the time scale ($\sim 9\times 10^{-14}$s) of the fragmentation process. In other words, the "internal $V\rightarrow T$" process is ineffective in spite of the fact that the excited state lifetime is long enough to permit a sufficient number of ν_2' oscillations to form a well developed vibrational structure. The localization of the terminal –N = O motion must then have interesting consequences for the NO fragment energy distribution. Unfortunately, as mentioned previously, since HONO coexists with NO and NO_2 (which is readily photolyzed to hot NO), we have not attempted to probe the NO fragment generated by HONO photolysis. We merely speculate here on its fate.

According to a calculation based on the impulse model mentioned earlier, the impulse-induced NO translation and rotation amount to 2437 and 2170 cm^{-1}, respectively. The large amount of calculated NO rotational energy compared with that computed for OH is, of course, a trivial consequence of the fact that the NO center of mass is much further away from the N atom than that of the OH from the central O atom. The validity of any such calculation for NO depends, as mentioned previously for OH, on the rigidity of the NO unit. In addition to the above mechanism, the NO fragment may derive its rotation from the O–N–O bending vibration ν_5' in the parent. A treatment similar to the one given previously for OH yields an average rotational energy of only 70 cm^{-1} from this source. The form of the distribution due to these mechanisms are however quite different, being Gaussian ($\langle E_R\rangle = 70\ cm^{-1}$) from ν_5' and relatively sharply peaked ($\langle E_R\rangle = 2170\ cm^{-1}$) due to the impulse. If these two mechanisms contribute to similar extents, the actual distribution will be a convolution of the two effects. It might show a slow ν_5'-induced rise and a relatively sharp falloff on the high energy wing originating predominantly from the impulse. Such a non-Maxwellian distribution has indeed been observed[42] recently in NO generated by the 355 nm photofragmentation of CH_3ONO, which is structurally similar to HONO. The significant contribution of the fragmentation impulse to the NO rotation might be indicative of the intuitively obvious fact that the doubly bonded NO in the parent is more rigid than the singly bonded OH unit. It is perhaps worth remarking here that considerations such as these reflect, to some extent, the artificiality of our treatment. A "complete" quantum analysis should obviate the necessity of using very loosely defined classical terms such as the rigidity of a bond.

The NO fragment vibrational distribution may be estimated on the basis of Franck–Condon arguments. The usual FC treatment[7] of photodissociation involves a sequence of events in which the fragmentation following the optical preparation of the upper state is "instantaneous", so that the parent retains its "memory" of the ground state wave function. This model has been used extensively in cases where the parent absorption spectrum does not show any vibrational structure, implying that dissociation is faster than the excited state internal motions. Since the fragmentation is thus instantaneous, the ground state wave function is influential since its projection on the upper state determines the initial ("$t = 0$") conditions in the "half-collision". However, in the case at hand, the HONO $\tilde{A}$ state survives long enough to permit a well developed vibrational (ν_2') structure. Thus it seems reasonable to make the simplifying assumption that, just before fragmentation, the parent does not retain much of its memory about its early ($\tilde{X}\,^1A'$) history. In other words, the

$\tilde{A}$–$\tilde{X}$ excitation serves merely as a method for preparing the $\tilde{A}$ state. The subsequent evolution into fragment vibrational states, in the absence of exit-channel effects, may then be calculated on the basis of a Franck–Condon treatment involving the fragments and the oscillators only in the $\tilde{A}$ state of the parent.

The quantity of interest is the probability of the process HONO $(\tilde{A}, r_{ON}, v_1 = 0, v_2) \rightarrow$ OH (X, v_{OH}) + NO (X, v_{NO}) + E_t where E_t is the final interfragment recoil energy. The probability P of a particular vibration-translation partitioning may be written as

$$P = |\langle \psi^{HONO}(r_{ON}, v_1 = 0, v_2) | \psi^{OH,NO}(E_t, v_{NO}, v_{OH}) \rangle|^2$$
$$= |\langle \psi_{r_{ON}} | \psi_t \rangle|^2 |\langle \psi^{v_2}_{HONO} | \psi^{v}_{NO} \rangle|^2 |\langle \psi^{v_1=0}_{HONO} | \psi^{v}_{OH} \rangle|^2. \quad (23)$$

Here $\psi_{r_{ON}}$ is the parent (continuum) wave function along the unstable coordinate r_{ON}; ψ_t refers to the fragment recoil and determines the final relative linear momentum through the deBroglie equation. The rest of the symbols have their obvious significance. In the above equations we have assumed the separability of the various coordinates. In addition, the rotational coordinates are completely ignored. However, as mentioned previously, the parent rotation plays a negligible role in the overall process; the OH fragment apparently derives its rotational energy predominantly from ν_3' and ν_6' in the parent and very little from the fragmentation impulse. The neglect of parent and OH fragment rotational coordinates in Eq. (23) is thus justified. On the other hand, the NO fragment apparently owes some of its rotation, as stated earlier, to the HO–NO recoil. However, since this is only a small fraction of the total available energy, the omission of the NO fragment rotational coordinate is not expected to be serious. The term $|\langle \psi^{v_1=0}_{HONO} | \psi^{v}_{OH} \rangle|^2$ sharply peaks at $v_{OH} = 0$ since, as mentioned in Sec. V, the equilibrium bond lengths in the parent and the fragment are nearly equal. The partitioning of the available energy into HO–NO recoil and NO fragment vibration is contained in the first two terms of Eq. (23).

We now calculate the NO fragment relative vibrational populations, given by $|\langle \psi^{v_2}_{HONO} | \psi^{v}_{NO} \rangle|^2$. Since the equilibrium NO bond lengths in the parent (1.28 Å) and the product (1.15 Å) are quite different, the Franck–Condon factors are nondiagonal. An accurate calculation of the vibrational distribution would require a detailed knowledge of the wave functions for the parent ν_2 vibration, which may be expected to be highly anharmonic. For convenience, however, we use harmonic oscillator wave functions for the localized NO oscillator in the parent as well as for the fragment. The results of such calculations are shown graphically in Fig. 10. The distributions are, of course, not expected to match reality in detail due to the neglect of vibrational anharmonicities. The only points we wish to make here are that (1) the distributions peak somewhat sharply at $v = 0$ for 2_0^1, 2_0^2, and 2_0^3 HONO excitations, and (2) the distribution is expected to be rather broad for the fragmentation of the vibrationless $\tilde{A}$ state. The former observation implies that the distribution of fragment velocities, given by $|\langle \psi_{r_{ON}} | \psi_t \rangle|^2$, should have a rather narrow spread with a sharp cutoff on the high velocity side. This is the same conclusion we reached previously (Sec. IV) from an analysis of the OH product Doppler profiles, independently of the above considerations.

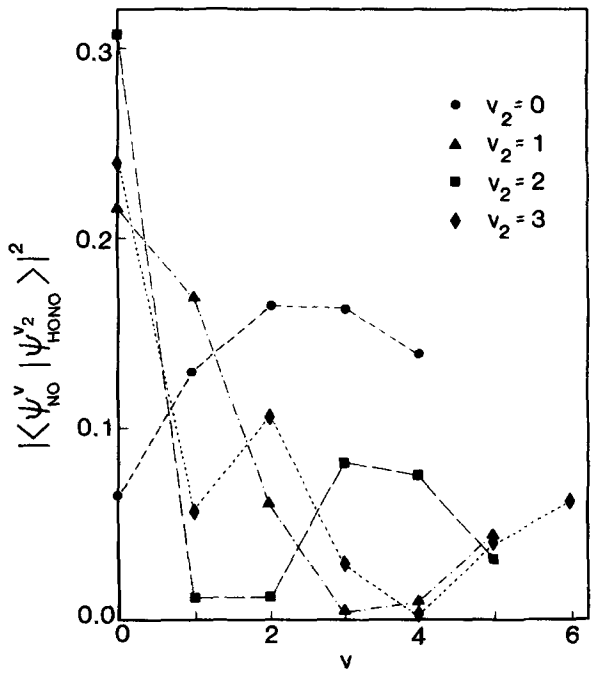

FIG. 10. The Franck–Condon factor $\langle \psi^{v}_{NO} | \psi^{v_2}_{HONO} \rangle^2$ as a function of v for various values of v_2. The calculation of the FC factor is based on harmonic oscillator wave functions for the local N = O oscillator in the parent as well as for the NO fragment. The high v cutoff in each case is determined by the available energy.

VII. THE HONO $\tilde{A}$ STATE SYMMETRY

In the work of King and Moule,[23] the HONO $\tilde{A}$ state symmetry (A'') was mainly inferred from the fact that the $\tilde{A}$–$\tilde{X}$ system has a low absorption cross section, implying a $\pi^* \leftarrow n$ transition. The conclusions of the present work provide the first unambiguous experimental proof for the A'' symmetry of the excited state. The first piece of evidence is the angular distribution of the ejected OH, as measured through the fragment Doppler profiles (Sec. IV). The anisotropy parameter β is close to the limiting value of -1, showing that the $\tilde{A}$–$\tilde{X}$ transition moment $\boldsymbol{\mu}$ is almost perpendicular to the central O–N bond. This conclusion, combined with the facts that the fragment alignment parameter $\mathscr{A}_0^{(2)}(R)$ is positive and that its trend agrees with calculation, establishes that $\boldsymbol{\mu}$ is close to being at right angles to the molecular frame and thus that the upper state symmetry is A''. This conclusion is in accord with the recent *ab initio* calculations of Larrieu, Dargelos, and Chaillet.[24]

VIII. DIRECT DISSOCIATION VS PREDISSOCIATION

It is interesting to speculate on the question of whether the upper state is short lived because of predissociation by another electronic state or because the diabatic $\tilde{A}$ state in itself is not bound along the dissociation coordinate ($\sim$the HONO internal coordinate r_{ON}).

We first consider electronic predissociation. On the basis of energetics, the only possible candidates are the $\tilde{X}\,^1A'$ and $\tilde{a}\,^3A''$ states. The singlet–triplet ($\tilde{A}$–$\tilde{a}$) interaction is too weak for a molecule composed of light atoms to result in a strong predissociation, although it could contribute to the OH photofragment F_2/F_1 population anomalies discussed

previously. Predissociation by the ground state is possible through the mechanism of vibronic coupling, induced by the out-of-plane torsional vibration $\nu_6'(a'')$. Since we do not excite ν_6' vibrations in the upper state, this coupling requires that each member of the 2^n progression interact with an $\tilde{X}$ state vibrational level containing odd quanta of ν_6''. The $\tilde{A}$–$\tilde{X}$ radiationless transition probability P may be written in terms of the interaction matrix element responsible for this coupling

$$P \propto |\langle \tilde{A},2^n|\mathscr{H}'|\tilde{X},6^m\rangle|^2/\Delta E^2. \quad (24)$$

Here $|\tilde{A},2^n\rangle$ and $|\tilde{X},6^m\rangle$ are, respectively, the coupled excited and ground state vibronic levels separated by ΔE, and $\mathscr{H}'$ is the nuclear kinetic energy operator. This mechanism for the $\tilde{A}$ state predissociation, however, implies that the predissociation rates for each member of the 2^n progression should be somewhat different because of the dependence on the energy dominator ΔE. This may be borne out by the slightly different widths of the individual 2_0^n vibronic bands although, experimentally, incomplete resolution of the $\tilde{A}$–$\tilde{X}$ *trans*-HONO vibronic features, because of blends with *cis*-HONO transitions, seem to obscure the unambiguous identifications of any such effect.

An alternative interpretation is that the diabatic $\tilde{A}$ state undergoes "direct dissociation". A single potential energy surface that is consistent with the experimental observations is the one which is repulsive along the r_{ON} internal coordinate but has a minimum along r_{NO} in the FC region. This trivial surface is schematically shown in Fig. 11(a) and, in a broad sense, corresponds to Herzberg's "type II" predissociation (i.e., a vibrational predissociation).[46] The $\tilde{A}$ state lifetime is, of course, determined predominantly by the slope of the repulsive wall. A variant, which may also be broadly classified as a vibrational predissociation, is slightly "flat" along r_{ON} *only* near the FC region [see Fig. 11(b)]. This form is suggested by the recent *ab initio* calculations of Larrieu, Dargelos, and Chaillet.[24] In this regard, the surface resembles the one proposed previously by Pack[47] to be responsible for the structured nature of many diffuse polyatomic spectra. As shown schematically in Fig. 11(b), the $\tilde{A}$ state surface is stable along r_{NO} but very unstable along r_{ON} except in the FC region where it is somewhat flat and thus has a pocket of quasistability. The $\tilde{A}$–$\tilde{X}$ vibronic structure arises due to local large amplitudes in the vibrational wave function in the flat region. The short upper state lifetime is essentially determined by the short transit time between the quasistable "dimple" and the very steep region leading to the products. Such surfaces explain the relative insensitivity of the OH fragment energy content to the number of ν_2 quanta in the parent. Fragmentation is along a predominantly steep coordinate and is thus not significantly perturbed by motion along r_{NO}.

IX. FUTURE PROSPECTS

Using laser spectroscopic techniques we have measured all the possible scalar and vectorial properties of a photofragment in considerable detail. In particular, we have probed the OH fragment ejected by the HONO $\tilde{A}$ state. This has been studied as a function of the terminal NO vibrational degree of freedom, which is the only one available through direct optical excitation. Such state-selected fragmentation studies are in general capable of providing at least qualitative ideas about the upper state relative slopes along different coordinates which may or may not influence the dissociation dynamics, as shown in Sec. VIII. There are complementary experiments[48,49] based on resonance Raman spectroscopy, which probe the geometrical changes that the parent undergoes "during" decomposition.[50] The latter approach would be quite interesting in the case of HONO, since this might allow one to explore upper state slopes along the vibrational coordinates not directly prepared by optical excitation.

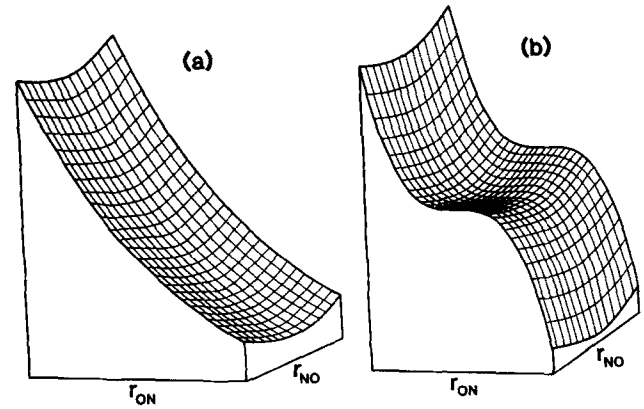

FIG. 11. Possible *qualitative* features of the HONO $\tilde{A}$ state potential energy surface, consistent with experimental observations (see the text).

It would be of considerable interest to characterize in detail the fate of NO photoejected by HONO. This would, of course, require the synthesis of HONO without contamination by significant quantities of NO_2 in particular. We note however that the crude (harmonic oscillator-based) calculations, summarized in Fig. 10, indicate that at least for the vibrationless $\tilde{A}$ state dissociation, some of the NO product might be vibrationally quite excited—more than that formed by NO_2 photolysis at the corresponding wavelength. Thus there is still some hope for being able to probe part of the NO ejected by the HONO $\tilde{A}$ state. It should also be worthwhile to probe the HONO(DONO) $\xrightarrow{h\nu}$H(D) + NO_2 channel through, e.g., H(D) fragment angular and velocity distributions especially since this process, as opposed to HONO $\xrightarrow{h\nu}$OH + NO, is thought to present a barrier to fragmentation.

It would also be of interest to investigate the decomposition of the HONO $\tilde{B}$ state, which is thought to be of A' symmetry. Here one could compare the product motion in this process, which takes place on the order of a few femtoseconds, with the present results. Since not much (especially the structure) is known about this state, the interpretation of the experimental data might be considerably aided by detailed *ab initio* calculations, which do not exist at present. It is also quite tempting to perform experiments on OH, NO inelastic scattering in order to test our proposal that such events in the exit channel might be responsible for the peculiar F_2/F_1 population ratio in OH produced by HONO ($\tilde{A}$) fragmentation.

We conclude by reiterating that the current study demonstrates how the mechanics of a photodissociation process can be elucidated in detail by determining the correlation between the fragment scalar and vectorial properties, i.e., between product translation, alignment, and internal state populations. We feel that the technique of combining Doppler and polarization laser excitation spectroscopy can be applied with unprecedented advantage to other chemical processes as well.

ACKNOWLEDGMENTS

The Nd:YAG laser used in this work was on loan from the San Francisco Laser Center, which is operated jointly by the University of California, Berkeley, and Stanford University and is supported by the National Science Foundation under grant CHE 79-16250. One of us (RNZ) gratefully acknowledges support of the National Science Foundation (NSF CHE 80-06524 and NSF PHY 82-06400) and of Shell Companies, Inc., through their Distinguished Chairs Program. RNZ and RND acknowledge the award of a NATO grant (141.82). RV would like to thank F. Lahmani, C. Lardeux, and D. Solgadi (CNRS, Paris) for generously sharing their experimental results on CH_3ONO photochemistry, C. Noda for his plotting routine used in simulating Fig. 10, and the National Science Foundation for a foreign travel grant under NSF INT TRAVEL 79-24367.

APPENDIX A: TRANSFORMATION OF PARENT VALENCE ANGLE BENDING MOTION INTO FRAGMENT IN-PLANE ROTATION

Consider a *trans* tetraatomic molecule ABCD which dissociates into AB and CD. We relate here the kinetic energy associated with the pseudorotation of the AB unit in ABCD, during the ABC angle bending vibration ν_3, to the vibrational frequency ω_3, the molecular geometry of the parent and to the masses of the constituent atoms. A convenient means for achieving this is through the "**s** vector" method.[51,52] Let s_t be a generic internal coordinate, which is the valence angle ϕ_1 [see Fig. 12(a)] in the case at hand. Then

$$s_t = \sum_{\alpha=1}^{N} \mathbf{s}_{t\alpha}\cdot\boldsymbol{\rho}_\alpha, \tag{A1}$$

where the components of the vector $\boldsymbol{\rho}_\alpha$ are the Cartesian displacements of the atom α. The kinetic energy T_v associated with the vibrational motion is

$$T_v = \tfrac{1}{2}\sum_{\alpha=1}^{N} \mu_\alpha s_{t\alpha}^2 \dot{s}_t^2, \tag{A2}$$

where $\mu_\alpha = 1/m_\alpha$, the reciprocal of the mass of the atom α. If the atom D is regarded as a spectator, the problem is reduced to that of a pseudotriatomic (ABC) system. The components of $\mathbf{s}_{t\alpha}$ for the bending vibration of a triatomic molecule are well known[51,52]:

$$\mathbf{s}_{t\mathrm{A}} = (\hat{\mathbf{e}}_{\mathrm{BA}}\cos\phi_1 - \hat{\mathbf{e}}_{\mathrm{BC}})/r_{\mathrm{AB}}\sin\phi_1 = \hat{\mathbf{e}}_{\mathrm{BA}}^{\perp}/r_{\mathrm{AB}}, \tag{A3}$$

$$\begin{aligned}\mathbf{s}_{t\mathrm{C}} &= (\hat{\mathbf{e}}_{\mathrm{BC}}\cos\phi_1 - \hat{\mathbf{e}}_{\mathrm{BA}})/r_{\mathrm{BC}}\sin\phi_1 \\ &= [(\sin\phi_1\hat{\mathbf{e}}_{\mathrm{BA}}^{\perp} + \cos\phi_1\hat{\mathbf{e}}_{\mathrm{BA}})\cos\phi_1 - \hat{\mathbf{e}}_{BA}]/r_{\mathrm{BC}}\sin\phi_1,\end{aligned} \tag{A4}$$

$$\begin{aligned}\mathbf{s}_{t\mathrm{B}} - \mathbf{s}_{t\mathrm{A}} - \mathbf{s}_{t\mathrm{C}} &= \frac{(r_{\mathrm{AB}} - r_{\mathrm{BC}}\cos\phi_1)\hat{\mathbf{e}}_{\mathrm{BA}} + (r_{\mathrm{BC}} - r_{\mathrm{AB}}\cos\phi_1)\hat{\mathbf{e}}_{\mathrm{BC}}}{r_{\mathrm{AB}}r_{\mathrm{BC}}\sin\phi_1} \\ &= \frac{(r_{\mathrm{AC}} - r_{\mathrm{BC}}\cos\phi_1)\hat{\mathbf{e}}_{\mathrm{BA}} + (r_{\mathrm{BC}} - r_{\mathrm{AB}}\cos\phi_1)(\sin\phi_1\hat{\mathbf{e}}_{\mathrm{BA}}^{\perp} + \cos\phi_1\hat{\mathbf{e}}_{\mathrm{BA}})}{r_{\mathrm{AB}}r_{\mathrm{BC}}\sin\phi_1}.\end{aligned} \tag{A5}$$

Here $\hat{\mathbf{e}}_{\mathrm{BA}}$ and $\hat{\mathbf{e}}_{\mathrm{BC}}$ are unit vectors directed along BA and BC, respectively; and $\hat{\mathbf{e}}_{\mathrm{BA}}^{\perp}$ is a unit vector perpendicular to BA [see Fig. 12(a)]. The rest of the symbols have their usual meanings.

The rotational energy of the AB unit, which is transformed into that of the fragment AB, is given by

$$2T_R = \frac{m_{\mathrm{A}}m_{\mathrm{B}}}{m_{\mathrm{A}} + m_{\mathrm{B}}}(\mathbf{s}_{t\mathrm{A}}\cdot\hat{\mathbf{e}}_{\mathrm{BA}}^{\perp}/m_{\mathrm{A}} - \mathbf{s}_{t\mathrm{B}}\cdot\hat{\mathbf{e}}_{\mathrm{BA}}/m_{\mathrm{B}})^2\dot{s}_t^2, \tag{A6}$$

where $\dot{s}_t$ is $\dot{\phi}_1$. From Eqs. (A2), (A3), (A5), and (A6) we find

$$\frac{T_R}{T_v} = \frac{1}{2}\frac{m_{\mathrm{A}}m_{\mathrm{B}}\{r_{\mathrm{BC}}/m_{\mathrm{A}} - [r_{\mathrm{AB}}\cos\phi_1 - r_{\mathrm{BC}}]/m_{\mathrm{B}}\}^2}{m_{\mathrm{AB}}\left\{r_{\mathrm{BC}}^2/m_{\mathrm{A}} + [r_{\mathrm{AB}}^2 - 2r_{\mathrm{AB}}r_{\mathrm{BC}}\cos\phi_1 + r_{\mathrm{BC}}^2]/m_{\mathrm{B}} + \dfrac{r_{\mathrm{AB}}^2}{m_{\mathrm{C}}}\right\}}. \tag{A7}$$

Substituting the harmonic oscillator relation $T_v = \omega_3(v_3 + \frac{1}{2})$ in Eq. (A7) leads to Eq. (9) for $v_3 = 0$.

APPENDIX B: TRANSFORMATION OF PARENT TORSIONAL MOTION INTO FRAGMENT OUT-OF-PLANE ROTATION

The **s** vectors for the internal coordinate associated with the torsional vibration, namely the dihedral angle τ between the bonds BA and CD [see Fig. 12(b)], are also given by Wilson, Decius, and Cross,[51] and by Califano[52]:

$$\mathbf{s}_{t\mathrm{A}} = \frac{-\hat{\mathbf{e}}_{\mathrm{AB}}\times\hat{\mathbf{e}}_{\mathrm{BC}}}{r_{\mathrm{AB}}\sin^2\phi_1} = \frac{-\hat{\mathbf{e}}_z^{\mathrm{ABC}}}{r_{\mathrm{AB}}\sin\phi_1}, \tag{A8}$$

$$\begin{aligned}\mathbf{s}_{t\mathrm{B}} &= \frac{r_{\mathrm{BC}} - r_{\mathrm{AB}}\cos\phi_1}{r_{\mathrm{BC}}r_{\mathrm{AB}}\sin\phi_1}\frac{\hat{\mathbf{e}}_{\mathrm{AB}}\times\hat{\mathbf{e}}_{\mathrm{BC}}}{\sin\phi_1} + \frac{\cos\phi_2}{r_{\mathrm{BC}}\sin\phi_2}\frac{\hat{\mathbf{e}}_{\mathrm{DC}}\times\hat{\mathbf{e}}_{\mathrm{CB}}}{\sin\phi_2} \\ &= \frac{r_{\mathrm{BC}} - r_{\mathrm{AB}}\cos\phi_1}{r_{\mathrm{BC}}r_{\mathrm{AB}}\sin\phi_1}\hat{\mathbf{e}}_z^{\mathrm{ABC}} + \frac{\cos\phi_2}{r_{\mathrm{BC}}\sin\phi_2}\hat{\mathbf{e}}_z^{\mathrm{BCD}},\end{aligned} \tag{A9}$$

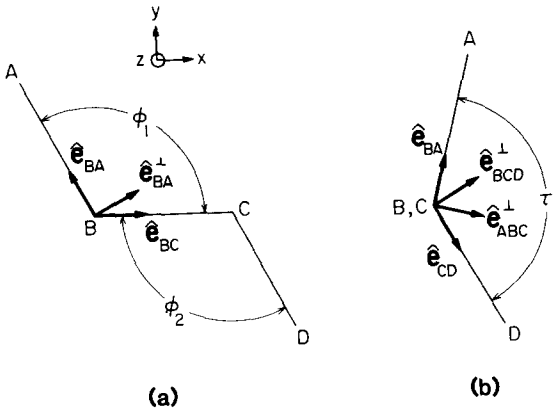

FIG. 12. The geometrical coordinates used in calculating the AB fragment rotation originating from (a) the in-plane ν_3 vibration, and (b) the out-of-plane torsion ν_6. The former motion is associated with the change of the valence angle ϕ_1, while the latter alters the dihedral angle τ between the AB and CD bonds.

$$\mathbf{s}_{tC} = \frac{r_{BC} - r_{CD}\cos\phi_2}{r_{BC} - r_{CD}\sin\phi_2}\,\frac{\hat{\mathbf{e}}_{DC}\times\hat{\mathbf{e}}_{CB}}{\sin\phi_2} + \frac{\cos\phi_1}{r_{BC}\sin\phi_1}\,\frac{\hat{\mathbf{e}}_{AB}\times\hat{\mathbf{e}}_{BC}}{\sin\phi_1} = \frac{r_{BC} - r_{CD}\cos\phi_2}{r_{BC} - r_{AB}\sin\phi_2}\,\hat{\mathbf{e}}_z^{BCD} + \frac{\cos\phi_1}{r_{BC}\sin\phi_1}\,\hat{\mathbf{e}}_z^{ABC}, \quad \text{(A10)}$$

$$\mathbf{s}_{tD} = \frac{-\hat{\mathbf{e}}_{DC}\times\hat{\mathbf{e}}_{CB}}{r_{CD}\sin^2\phi_2} = \frac{-\hat{e}_z^{BCD}}{r_{AB}\sin\phi_2}, \quad \text{(A11)}$$

where

$$\frac{\hat{\mathbf{e}}_{AB}\times\hat{\mathbf{e}}_{BC}}{\sin\phi_1} = \hat{\mathbf{e}}_z^{ABC}$$

and

$$\frac{\hat{\mathbf{e}}_{DC}\times\hat{\mathbf{e}}_{CB}}{\sin\phi_2} = \hat{\mathbf{e}}_z^{BCD}$$

are unit vectors perpendicular to the ABC and BCD planes [see Fig. 12(b)]. For a *trans*-planar tetraatomic molecule, $\tau = 180°$, so that $\hat{\mathbf{e}}_z^{ABC} = \hat{\mathbf{e}}_z^{BCD}$.

Just as for the ν_3-induced AB rotation, T_v is again given by Eq. (A2). The rotational kinetic energy of AB has an expression analogous to Eq. (A6):

$$2T_R = \frac{m_A m_B}{m_A + m_B}\,(s_{tA}/m_A - s_{tB}/m_B)^2\dot{s}_t^2, \quad \text{(A12)}$$

where $\dot{s}_t$ is $\dot{\tau}$.

From Eqs. (A2), (A8), (A9), and (A12) we find

$$\frac{T_R}{T_v} = \frac{m_A m_B\{r_{BC}\sin\phi_2/m_A + [r_{AB}\sin(\phi_1-\phi_2) + r_{BC}\sin\phi_2]/m_B\}^2 r_{CD}^2}{2m_{AB}\{[r_{BC}r_{CD}\sin\phi_2]^2/m_A + r_{CD}^2[r_{AB}\sin(\phi_1-\phi_2) + r_{BC}\sin\phi_2]^2/m_B + r_{AB}^2[r_{BC}\sin\phi_1 - r_{CD}\sin(\phi_1-\phi_2)]^2/m_C + [r_{AB}r_{BC}\sin\phi_1]^2/m_B\}}. \quad \text{(A13)}$$

Substitution of $T_v = \omega_6(v_6 + \frac{1}{2})$ into Eq. (A13) leads to Eq. (11) for $v_6 = 0$.

[1]K. R. Wilson, in *Excited State Chemistry*, edited by J. N. Pitts (Gordon and Breach, New York, 1970).
[2]J. P. Simons, *Specialist Periodical Report, Gas Kinetics and Energy Transfer* (Chemical Society, London, 1977), Vol. 2, p. 56.
[3]R. N. Zare and D. R. Herschbach, Proc. IEEE **51**, 173 (1963).
[4]M. Shapiro and R. Bersohn, Annu. Rev. Phys. Chem. **33**, 409 (1982).
[5]K. E. Holdy, L. C. Klotz, and K. R. Wilson, J. Chem. Phys. **52**, 4588 (1970).
[6]Y. B. Band and K. F. Freed, J. Chem. Phys. **63**, 3382 (1975); **67**, 1462 (1977); **68**, 1292 (1978); M. D. Morse, K. F. Freed, and Y. B. Band, *ibid.* **70**, 3604 (1979).
[7]K. F. Freed, M. D. Morse, and Y. B. Band, Discuss. Faraday Soc. **67**, 297 (1979); M. D. Morse and K. F. Freed, J. Chem. Phys. **78**, 6045 (1983).
[8]C. H. Greene and R. N. Zare, Annu. Rev. Phys. Chem. **33**, 119 (1982).
[9]R. Vasudev and R. N. Zare, J. Chem. Phys. **76**, 5267 (1982).
[10]J. M. Brown and D. A. Ramsay, Can. J. Phys. **53**, 2232 (1975).
[11]S. Michelson, A. J. Merer, S. A. Rice, F. A. Novak, K. F. Freed, and Y. Hamada, J. Chem. Phys. **74**, 3089 (1981).
[12]P. A. McDonald and K. K. Innes, Chem. Phys. Lett. **59**, 562 (1978).
[13]K. Evans, R. Scheps, S. A. Rice, and D. Heller, J. Chem. Soc. Faraday Trans. 2 **69**, 856 (1973).
[14]G. Ondrey, S. Kaufer, and R. Bersohn, J. Chem. Phys. **79**, 179 (1983).
[15]J. Pfab, J. Häger, and W. Krieger, J. Chem. Phys. **78**, 266 (1983).
[16]J. B. Halpern and W. M. Jackson, J. Phys. Chem. **86**, 973 (1982).
[17]G. Ondrey, N. van Veen, and R. Bersohn, J. Chem. Phys. **78**, 3732 (1983).
[18]C. H. Greene and R. N. Zare, J. Chem. Phys. **78**, 674 (1983).
[19]P. Andresen, and E. W. Rothe, J. Chem. Phys. **78**, 989 (1983); P. Andresen, G. S. Ondrey, B. Titze, and E. W. Rothe, *ibid.* (submitted).
[20]This problem has been considered in the case of an electronically excited fragment (Ref. 8): J. A. Guest, M. A. O'Halloran, and R. N. Zare, Chem. Phys. Lett. **103**, 261 (1984). Preliminary results of this work were presented at the NATO ASI Meeting on Photophysics and Photochemistry in the Vacuum Ultraviolet, Lake Geneva, Wisconsin, 1982.
[21]J. P. Simons and A. J. Smith, Chem. Phys. Lett. **97**, 1 (1983).
[22]R. Vasudev, R. N. Zare, and R. N. Dixon, Chem. Phys. Lett. **96**, 399 (1983).
[23]G. W. King and D. Moule, Can. J. Chem. **40**, 2057 (1962).
[24]C. Larrieu, A. Dargelos, and M. Chaillet, Chem. Phys. Lett. **91**, 465 (1982).
[25]R. C. Mitchell and J. P. Simons, Discuss. Faraday Soc. **44**, 208 (1967).
[26]R. P. Mariella and A. C. Luntz, J. Chem. Phys. **67**, 5388 (1977); R. P. Mariella, B. Lantzsch, V. T. Maxson, and A. C. Luntz, *ibid.* **69**, 5411 (1978).
[27]W. D. Gwinn, B. E. Turner, W. M. Goss, and G. L. Blackman, Astrophys. J. **179**, 789 (1973); M. Bertojo, A. C. Cheung, and C. H. Townes, *ibid.* **208**, 914 (1976).
[28]J. M. Brown, J. T. Hougen, K.-P. Huber, J. W. C. Johns, I. Kopp, H. Lefebvre-Brion, A. J. Merer, D. A. Ramsay, J. Rostas, and R. N. Zare, J. Mol. Spectrosc. **55**, 500 (1975).
[29](a) F. Alberti and A. E. Douglas, Chem. Phys. **34**, 399 (1978); (b) A. M. Quinton and J. P. Simons, Chem. Phys. Lett. **81**, 214 (1981).
[30]A. Jacobs, K. Kleinermanns, H. Kuge, and J. Wolfrum, J. Chem. Phys. **79**, 3162 (1983).
[31]A. F. Tuck, J. Chem. Soc. Faraday Trans. **2**, 689 (1977).
[32]See, for example, S. A. Rice, in *Advances in Laser Chemistry*, edited by A. Zewail (Springer,Berlin, 1978).
[33]J. A. Silver, W. L. Dimpfl, J. H. Brophy, and J. L. Kinsey, J. Chem. Phys. **65**, 1811 (1976).
[34]R. Varma and R. F. Curl, Jr., J. Phys. Chem. **82**, 402 (1976).
[35]I. L. Chidsey and D. R. Crosley, J. Quant. Spectrosc. Radiat. Transfer **23**, 187 (1980).
[36]The "rotational temperature" reported earlier (Ref. 22) for the F_1 component was obtained from $Q_1 + {}^QP_{21}$ intensities and thus refers to the

$X\,^2\Pi_{3/2}^{-}$ Λ-doublet component.

[37]R. Schmiedl, H. Dugan, W. Meier, and K. H. Welge, Z. Phys. A **304**, 137 (1982).

[38]The limiting value of $\beta = -1$ is strictly valid only in the limit of, among other things, the fragmentation being infinitely faster than molecular rotation. The estimated $\tilde{A}$ state lifetime, as mentioned previously, is $\sim 9\times 10^{-14}$s. Calculations based on this lifetime and the HONO rotational period, together with the assumptions of a delta function distribution of fragment recoil velocities and the parent transition moment being exactly perpendicular to the O–N bond, give an effective β of ~ -0.99. The effect of finite lifetime on β due to parent rotation is thus negligible.

[39]In our preliminary report (Ref. 22) on the 369 nm photolysis, we assumed that the fraction of E_a available to OH includes the contribution from the vibrational (2^1) energy initially deposited in $-$ N = O. The present results indicate that this nonadiabatic assumption is not correct.

[40]See also M. H. Alexander and P. J. Dagdigian, J. Chem. Phys. (submitted).

[41]Since we have established the importance of the HONO zero-point bending motions in the generation of OH rotation, it may be argued that the slight apparent "blurring" of the fragment angular distribution (effective $\beta > -1.0$), discussed previously in Sec. IV, could be attributed partly to these vibrations. The effect of these motions may be visualized in terms of the associated pseudorotation of the central O–N unit, resulting in a "smearing out" of the initial O–N,$\hat{\epsilon}_p$ alignment established by the $\tilde{A}$–$\tilde{X}$ excitation. Calculations based on this mechanism combined with effects due to the parent rotation (Ref. 38), give $\beta = -0.95$. Thus it appears that the effect of these mechanisms is not very significant and the lowering of the central contrast in the OH fragment Doppler profiles (see Sec. IV) is probably mostly due to a small distribution of recoil velocities.

[42]F. Lahmani, C. Lardeux, and D. Solgadi, Chem. Phys. Lett. **102**, 523 (1983).

[43]D. R. Yarkony, H. F. Schaefer, and S. Rothenberg, J. Am. Chem. Soc. **96**, 656 (1974).

[44]D. K. Russell and H. E. Radford, J. Chem. Phys. **72**, 7250 (1980).

[45]Although it may be dangerous to generalize this to include other systems in the absence of experimental measurements on both fragments, it is interesting that such spin-orbit population anomalies have also been observed in the case of NO_2 photodissociation [H. Zacharias, M. Geilhampt, K. Meier, and K. H. Welge, J. Chem. Phys. **74**, 218 (1981); A. P. Baronowskii, B. M. DeKoven, and H. Helvajian, XV Informal Conference on Photochemistry, Stanford University, California, 1982]. Here again the spin-orbit splitting in the NO fragment ($X\,^2\Pi_{3/2}$–$X\,^2\Pi_{1/2} \simeq 125$ cm^{-1}) is similar in magnitude to that in atomic oxygen fragment ($^3P_2 - {}^3P_1 \simeq -160$ cm^{-1}) but opposite in sign. Further support for this interpretation is provided by the recent study of $HONO_2$ photolysis in which the OH F_1 and F_2 components are statistically populated (Ref. 30). Here the spin splittings in the two fragments are quite mismatched.

[46]G. Herzberg, *Molecular Spectra and Molecular Structure* (Van Nostrand, New York, 1966), Vol. III.

[47]R. T Pack, J. Chem. Phys. **65**, 4765 (1976).

[48]P. A. Hackett, R. A. Back, and S. Koda, J. Chem. Phys. **65**, 5103 (1976).

[49]D. G. Imre, J. L. Kinsey, R. W. Field, and D. H. Katayama, J. Phys. Chem. **86**, 2564 (1982).

[50]E. J. Heller, J. Chem. Phys. **62**, 1544 (1975); S.-Y. Lee and E. J. Heller, *ibid.* **71**, 4777 (1979).

[51]E. B. Wilson, Jr., J. C. Decius, and P. C. Cross, *Molecular Vibrations* (Dover, New York, 1955).

[52]S. Califano, *Vibrational States* (Wiley, New York, 1976).